

## Boundary Layer Energy Transport and Cumulus Development over a Heated Mountain: An Observational Study

J. CORY DEMKO, BART GEERTS, AND QUN MIAO

*University of Wyoming, Laramie, Wyoming*

JOSEPH A. ZEHNDER

*Creighton University, Omaha, Nebraska*

(Manuscript received 27 November 2007, in final form 2 July 2008)

### ABSTRACT

Aircraft and surface measurements of the boundary layer transport of mass and moisture toward an isolated, heated mountain are presented. The data were collected around the Santa Catalina Mountains in Arizona, 20–30 km in diameter, during the North American monsoon, on days with weak winds and cumulus congestus to cumulonimbus development over the mountain. Flights in the boundary layer around the mountain and surface station data indicate that mountain-scale anabatic surface wind generally develops shortly after sunrise, peaking at  $\sim 1 \text{ m s}^{-1}$  in strength close to solar noon. There is some evidence for a toroidal heat island circulation, with divergence in the upper boundary layer. The aircraft data and mainly the diurnal surface temperature and pressure patterns confirm that this circulation is driven by surface heating over the mountain. Three case studies suggest that growth spurts of orographic cumulus and cumulonimbus are not preceded by enhanced mountain-scale mass convergence near the surface, and that the decay of orographic deep convection is associated with divergence around the mountain.

### 1. Introduction

It is well-known that cumulus convection erupts almost daily close to solar noon over the mountains in the interior western United States during the summer. Most introductory meteorology textbooks display schematics of topographically induced, thermally forced circulations over mountains (e.g., Ackerman and Knox 2007, p. 365; Aguado and Burt 2007, p. 238). Even relatively simple numerical simulations have shown that under sufficient solar radiation forcing, weak stratification, and weak wind, a thermally direct circulation develops over a mountain, with anabatic flow converging over the mountain, as illustrated in Fig. 1 (e.g., Thyer 1966; McNider and Pielke 1981; Bader and Mckee 1983; Banta 1986). This is referred to as a “toroidal” circulation, because the horizontal vorticity forms a ring (or toroid) around the mountain.

However, few observations have been able to confirm the existence of such circulation, and studies gen-

erally only document the surface component (e.g., Fujita et al. 1962; Garrett 1980; Banta 1984; Vergeiner and Dreiseitl 1987; Whiteman 1990; Hernández et al. 1998). And, to our knowledge, there are no studies that have linked convective development to the evolution of near-surface convergence around a mountain, although a number of aircraft experiments have focused on flight-level observations of convergent orographic flow and cumulus formation over the Magdalena Mountains in New Mexico (e.g., Braham and Draginis 1960; Raymond and Wilkening 1980, 1982, 1985). The daytime anabatic circulation is distinctly different and more complex than the katabatic flow. The katabatic (or drainage) flow is a shallow gravity current concentrated in valleys and is commonly present around dawn. The anabatic flow has received little attention compared to the katabatic flow, both observationally and numerically, yet it is more important in terms of cloud and precipitation development and interactions between the convective boundary layer (CBL) and the free troposphere.

The anabatic circulation may be hard to detect because of the intense mixing within the CBL. Convective turbulence may mix the anabatic momentum over a

---

*Corresponding author address:* Bart Geerts, Department of Atmospheric Sciences, University of Wyoming, Laramie, WY 82071.  
E-mail: geerts@uwyo.edu

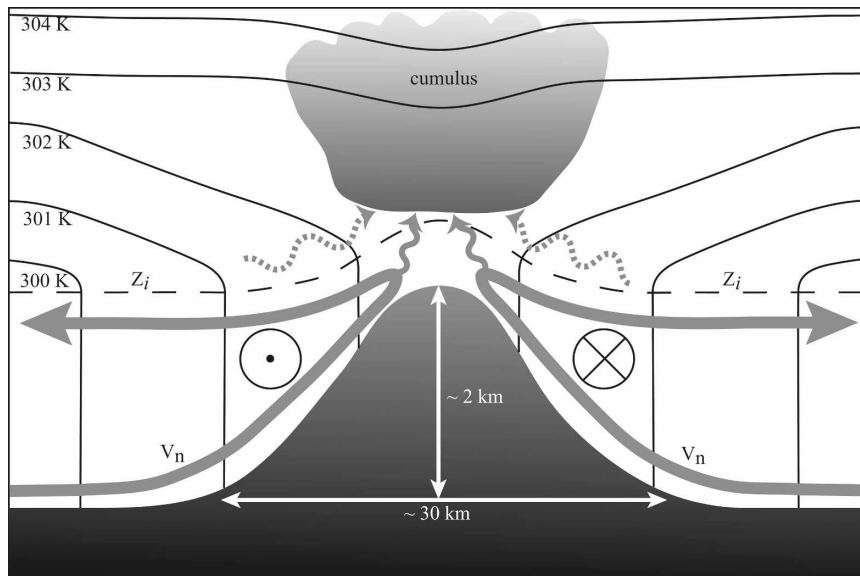


FIG. 1. Schematic transect of the boundary layer flow (labeled  $v_n$ ), convective boundary layer depth ( $z_i$ , dashed line), temperature distribution, and cumulus development over an isolated, heated mountain without large-scale wind. The thin solid lines are isentropes, starting with an arbitrary value of 300 K. The horizontal vorticity is shown as a vector pointing (left) out of and (right) into the transect. Part of the solenoidal circulation feeds the orographic cumulus cloud (solid wavy lines). The dashed wavy lines indicate convergent flow above the CBL, due to the warm anomaly over the mountain.

considerable depth, and the ascending flow in thermals is far stronger than the mountain-scale updraft due to net anabatic flow. The CBL develops as a result of a positive surface sensible heat flux, both over mountains and the surrounding plains. The CBL topography over complex terrain is poorly understood, but the afternoon CBL depth usually exceeds the mountain-top height in the western United States during the warm season. If the CBL remains capped by a stable layer, the toroidal circulation remains contained within the CBL (e.g., Banta 1984). When the capping is weaker, and sufficient low-level moisture is present, this circulation can lead to orographic cumulus convection, and an unknown part of the mountain-scale circulation is carried up through the cloud base and detrained at higher levels in the free troposphere (Fig. 1). This vertical transfer is concentrated into a number of vigorous buoyant cumuli smaller in width than the mountain. Buoyant cumulus convection may enhance the mountain-scale convergence near the surface, and maturing convection may suppress the convergence (e.g., Raymond and Wilkening 1982). Thus, several orographic cumulus growth cycles are possible in a single day, as has been observed (e.g., Zehnder et al. 2006). The key distinction of orographic convection is that the BL convergence does not advect with the mean flow.

The purpose of this observational study is to docu-

ment the evolution and vertical profile of anabatic flow (and associated heat convergence) over an isolated mountain, to examine the flow's thermal forcing, and to relate the flow to orographic cumulus development. The mountain studied herein is 20–30 km in diameter, thus the thermally forced circulation can be classified as a “mountain–plain” circulation rather than a “slope” wind, as defined in Whiteman (2000, p. 171).

Thermally forced orographic convergence and associated deep convection are essential to warm-season precipitation and to surface–troposphere exchange in regions with complex terrain. Because the mountains that drive the localized CBL convergence and deep convection are often small compared to model resolution, their impact on surface precipitation and deep-tropospheric conditions is poorly predicted by current numerical weather prediction (NWP) models (e.g., Bright and Mullen 2002). Even NWP models of sufficient resolution to resolve the thermally direct orographic circulations are challenged in their ability to simulate the surface fluxes and CBL development over complex terrain, and thus to predict the timing and intensity of ensuing thunderstorms (e.g., Yu et al. 2006).

Sections 2 and 3 discuss the data sources and analysis method, respectively. Observations are summarized in section 4. Section 5 examines the forcing of anabatic flow and its relationship with cumulus convection.

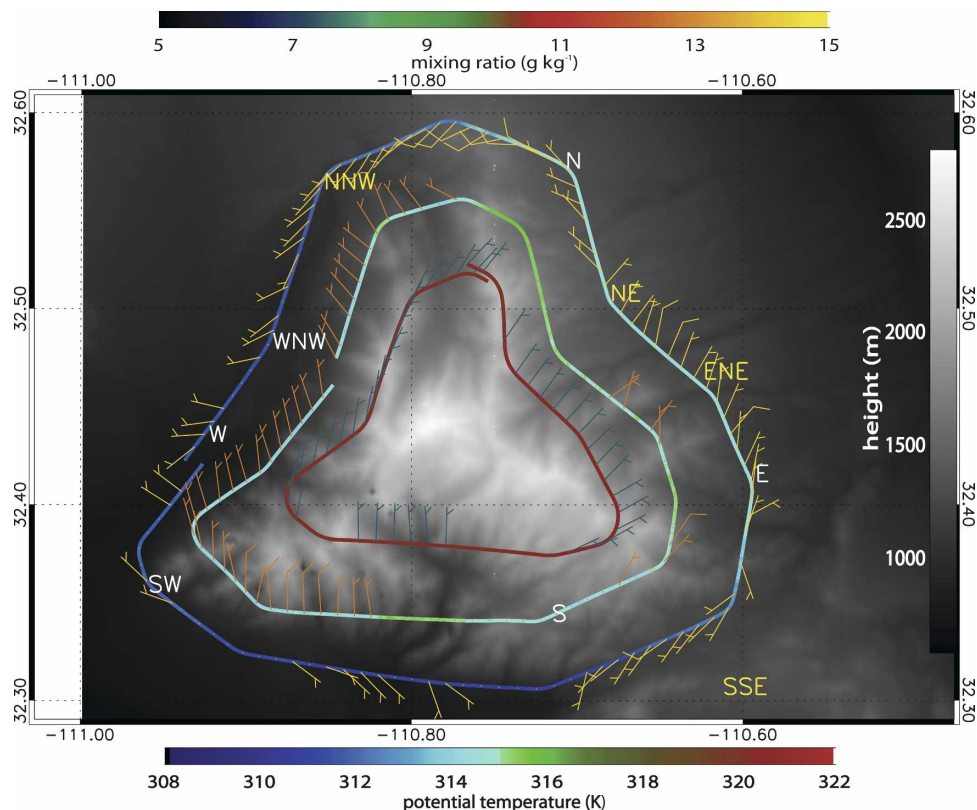


FIG. 2. Flight-level winds, potential temperature  $\theta$ , and mixing ratio  $r$  on three WKA circumnavigation legs between 1600 and 1648 UTC 25 Jul 2006. The grayscale shows the topography (m). Mt. Lemmon, near the center of the three loops, is 2797 m high. The WKA track is colored by flight-level  $\theta$ . The flight-level wind is shown with barbs; a full barb is  $5 \text{ m s}^{-1}$ . These barbs are colored by  $r$ . The ISFF stations are labeled in white (standard stations) and yellow (eddy flux towers).

## 2. Data sources

The data used in this study were collected as part of the Cumulus Photogrammetric, In situ and Doppler Observations (CuPIDO) campaign during the 2006 monsoon season around the Santa Catalina Mountains (SCM) in southeast Arizona (Damiani et al. 2008; all CuPIDO data are archived online at <http://www.eol.ucar.edu/projects/cupido/>). This mountain range has a horizontal scale of 20–30 km and a vertical scale of ~2000 m above the surrounding plains. Sixteen days were selected, each with orographic cumulus development, aircraft data, soundings, and surface meteorological data (see Table 1 in Damiani et al. 2008). We mainly examine data from the three of these 16 days with the best aircraft data. The University of Wyoming King Air (WKA) aircraft measured winds, state variables, and humidity at sufficient frequency to compute vertical fluxes. Mobile GPS Advanced Upper-Air Sounding System (MGAUS) sondes were released at 45–90-min intervals during WKA flights, from a location just upstream of the mountain top. Ten automated

surface meteorological stations were positioned around the mountain (Fig. 2). All measured basic meteorological variables at 1 Hz; 5-min averages are used in this study. Temperature and humidity was measured at 2 m, wind at 10 m AGL. Four stations were located on sufficiently level and homogenous ground that surface heat fluxes could be computed using the eddy correlation method, from data at 7 m AGL. The 4-station, 30-min average sensible and latent heat flux is denoted by SH and LH, respectively. We also use meteorological data from a tower located on Mt. Bigelow on the SCM spine, and from an astronomical observatory on Mt. Lemmon, the highest point of the SCM.

The evolution of orographic cumuli was captured by two pairs of digital cameras, one 30 km southwest of Mt. Lemmon and one 20 km northwest of Mt. Lemmon. Each camera in the pair was suitably spaced for stereophotogrammetry, and thus cloud edges can be geolocated at high temporal resolution (Zehnder et al. 2007). This method was used to obtain the cloud-top chronology (i.e., the evolution of the highest cumulus cloud top over the SCM).

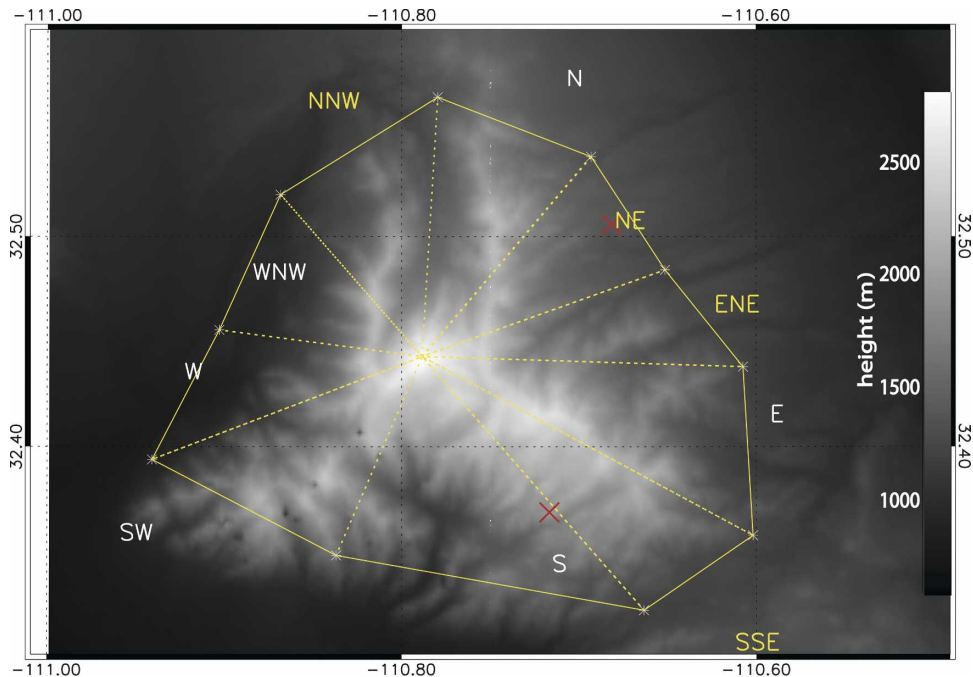


FIG. 3. Definition of the station polygon (solid yellow lines), based on midpoints between surface stations. The red crosses represent sounding launch sites for 19 and 25 Jul and 6 Aug 2006 (Windy Point near station S and Stratton Canyon at station NE).

The WKA circumnavigated the SCM 51 times on 16 flight days during CuPIDO. About half (24) of the flights followed an outer fixed track at  $300 \pm 30$  m AGL. Two other fixed tracks were flown: a middle loop at 780 hPa, which is about 640 m below mountain top; and an inner loop at 700 hPa, which is about 270 m above mountain top.

An example of three successive loops at these three flight levels is shown in Fig. 2. At most but not all places along the outer loop, the wind is directed toward the mountain (i.e., it has an anabatic component). The mean anabatic wind speed along the outer loop is  $0.9 \text{ m s}^{-1}$ . Variations exist along this loop (e.g., the potential temperature  $\theta$  is generally higher on the east side of the mountain at this time, some 4 h after sunrise, and the mixing ratio  $r$  is generally higher on the west side, where numerous well-watered golf courses are located). The inner loop (700 hPa) appears to be above the CBL at this time, because both  $\theta$  is higher and  $r$  is lower. Also, the flow along this loop is not clearly convergent, although there is still a weak anabatic component on average, superimposed on a  $2.8 \text{ m s}^{-1}$  mean northeast wind.

### 3. Analysis method

Both the flight loops and the positioning of the surface stations around the SCM allow us to calculate the

mountain-wide mass, heat, and moisture budgets. The method used here is similar to that used by Raymond and Wilkening (1980) for dry orographic circulations and Raymond and Wilkening (1982) for orographic cumulus. The mass convergence MC ( $\text{kg m}^{-1} \text{ s}^{-1}$ ) is defined as

$$\text{MC} = \oint \rho v_n ds, \quad (1)$$

where  $v_n$  ( $\text{m s}^{-1}$ ) is the wind component normal to the track, positive toward the mountain,  $\rho$  ( $\text{kg m}^{-3}$ ) is the air density, and  $ds$  (m) is the incremental distance along the line integral. For aircraft data, 1-Hz data are used, giving a  $ds$  value of  $\sim 90$  m. For station data,  $ds$  is the distance between the midpoints between stations (Fig. 3), and  $v_n$  is the wind component normal to  $ds$  at the station between these midpoints. We then use the divergence theorem (Holton 2004; Johnson and Priednitz 1981) to estimate the mean convergence within the aircraft loop or the station polygon (Fig. 3) with area  $A$  ( $\text{m}^2$ ):

$$A^{-1} \oint v_n ds = -\nabla \cdot \mathbf{v}_h. \quad (2)$$

Here  $\mathbf{v}_h$  is the horizontal wind vector. A convergence profile can be converted to a mean updraft  $\bar{w}$  ( $\text{m s}^{-1}$ ) within the loop:

$$\bar{w} = \frac{1}{Ag\rho_p} \int_p^{p_0} \left( \oint v_n ds \right) dp. \quad (3)$$

This assumes anelastic continuity and  $\bar{w} = 0$  at the surface. The integral bounds are the surface pressure  $p_o$  and the flight level pressure  $p$  (Pa). Area  $A$  is computed as the sum of the areas of triangles defined by a base  $ds$  and a corner at Mt. Lemmon. These triangles are shown in Fig. 3 for the station polygon area. The area is 576 km<sup>2</sup> for the station polygon, and about 739, 399, and 219 km<sup>2</sup> for the 300 m AGL, 780-, and 700-hPa WKA loops, respectively.

The mean inflow  $\bar{v}_n$  (m s<sup>-1</sup>), referred to as the anabatic flow speed, is computed as follows:

$$\bar{v}_n = \frac{1}{C} \oint v_n ds, \quad (4)$$

where  $C = \oint ds$  is the loop length, ranging from 52 km for the inner loop to 102 km for the outer loop (Fig. 2). The uncertainty in  $\bar{v}_n$  [i.e., the square root of the error variance  $\sigma^2(\bar{v}_n, C)$ ], can be estimated as follows for continuous aircraft measurements (Lenschow et al. 1999):

$$\sigma^2(\bar{v}_n, C) = 2\sigma_v^2 \frac{\ell_{vx}}{C}. \quad (5)$$

Here  $\ell_{vx}$  is the integral length scale of  $v_n$  along the flight path and  $\sigma_v^2$  is the error variance of  $v_n$ . According to Lenschow and Stankov (1986), the integral scale for horizontal velocity components measured within the CBL with depth  $z_i$  is  $\ell_{vx} = 0.45z_i$ . The gust probe velocity error variance is at most 1 m<sup>2</sup> s<sup>-2</sup>. Assuming  $z_i = 2$  km, we obtain a conservative estimate for the uncertainty in  $\bar{v}_n$  of  $0.13 < \sigma(\bar{v}_n, C) < 0.19$  m s<sup>-1</sup>. The appendix in Raymond and Wilkening (1985) contains a more rigorous error analysis of gust probe winds in terms of the aircraft slip angle and the angle of attack. A similar uncertainty for  $\bar{v}_n$  ( $\sim 0.18$  m s<sup>-1</sup>) is obtained for their circum-mountain flight pattern, which has about the same length. Raymond and Wilkening (1982) discuss an additional source of error in  $v_n$ , that is due to the Schuler oscillation of the inertial platform. This yields an uncertainty in  $\bar{v}_n$  of 0.1 m s<sup>-1</sup> for the outer loop (our worst case).

The error variance of  $\bar{v}_n$  from instantaneous station measurements can be estimated as (Lenschow et al. 1999):

$$\sigma^2(\bar{v}_n, L) = \sigma_v^2 \frac{\Delta}{C} = 0.1\sigma_v^2, \quad (6)$$

where  $\Delta$  is the typical distance between the 10 stations in the polygon. For 5-min-average wind estimates from prop-vane anemometers on a 10-m tower,  $\sigma_v$  is at most 0.33 m s<sup>-1</sup>, so the uncertainty in  $\bar{v}_n$  is 0.10 m s<sup>-1</sup>, which is comparable to that from the aircraft data. As will be shown later, aircraft and station data yield a typical magnitude of  $\bar{v}_n$  of 1 m s<sup>-1</sup> (i.e., a magnitude larger than its uncertainty).

The mean (advective) wind  $\mathbf{v}_m$  is defined as the vector mean wind along the track. Its magnitude will be compared to  $\bar{v}_n$ , to assess whether the flow primarily passes over/around the mountain, or is drawn toward the mountain.

We aim to quantify the horizontal flux convergence of mass and energy over the mountain, and place this in the context of changes in moist static energy over the mountain. Moist static energy  $h$  is defined as  $h \equiv \pi\theta + gz + L_vq$ , where  $\pi$  is the Exner function (J kg<sup>-1</sup> K<sup>-1</sup>),  $\pi = c_p T/\theta = c_p(p/p_o)^{R/c_p}$ ,  $c_p$  (J kg<sup>-1</sup> K<sup>-1</sup>) is the specific heat under constant pressure,  $R$  (J kg<sup>-1</sup> K<sup>-1</sup>) is the ideal gas constant for dry air,  $p_o = 1000$  hPa,  $\theta$  (K) is the potential temperature,  $T$  (K) is the temperature,  $g$  (m s<sup>-2</sup>) is gravity,  $z$  (m) is height,  $L_v$  (J kg<sup>-1</sup>) is the latent heat of condensation, and  $q$  (kg kg<sup>-1</sup>) is the specific humidity. The conservation equation of  $h$ , for inviscid flow, implies [e.g., Batchelor 1967, Eq. (3.1.16)]:

$$\frac{\partial \rho h}{\partial t} + \nabla \cdot (\rho h \mathbf{v}) = S. \quad (7)$$

Here  $\rho$  (kg m<sup>-3</sup>) is air density,  $\mathbf{v}$  is the 3D wind vector, and  $S$  (W m<sup>-3</sup>) is a diabatic heat source other than that due to condensation/evaporation (e.g., radiative heat convergence). Integration of (7) over area  $A$  gives

$$\int_A \int \frac{\partial \rho h}{\partial t} dA = \oint \rho h v_n ds - \int_A \int \frac{\partial \rho h w}{\partial z} dA + \int_A \int S dA. \quad (8)$$

The first term on the right of (8) is the horizontal flux convergence. This line integral, derived using the 2D divergence theorem, is computed over the closed loop defined by the station polygon (Fig. 3) or the WKA flight loops (Fig. 2). This term is not preceded by a minus sign because the line-normal flow  $v_n$  is defined as positive toward the mountain. The second term on the right in (8) denotes the vertical flux convergence. Substitution of the definition of  $h$  in (8) yields

---


$$\underbrace{\int_A \int \frac{\partial(\rho h)}{\partial t} dA}_{\text{I}} = \underbrace{\oint \pi \rho \theta v_n ds}_{\text{II}} + \underbrace{\oint L_p q v_n ds}_{\text{III}} + \underbrace{\oint g p z v_n ds}_{\text{IV}} - \underbrace{\int_A \int \frac{\partial(\rho h w)}{\partial z} dA}_{\text{V}} + \underbrace{\int_A \int S dA}_{\text{VI}}. \quad (9)$$

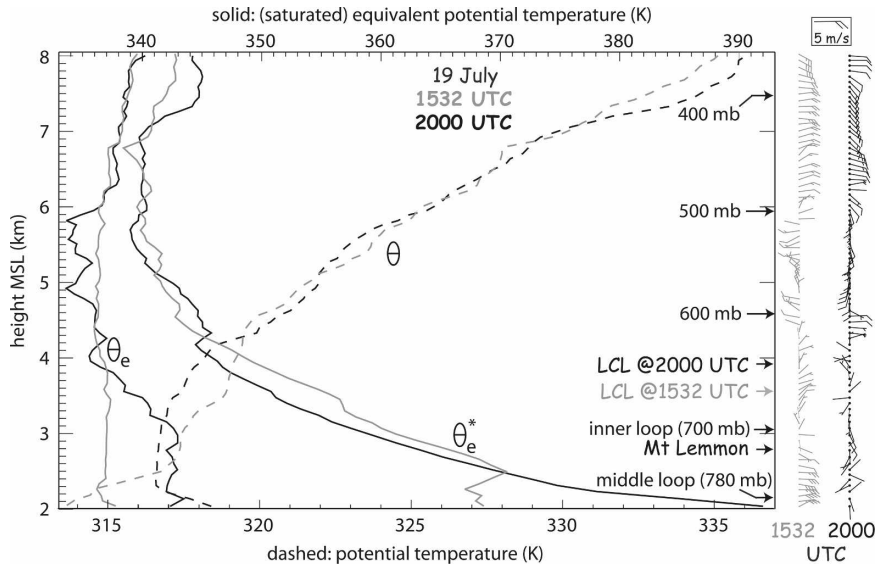


FIG. 4. Profiles of  $\theta$ ,  $\theta_e$ ,  $\theta_e^*$ , and wind at 1532 (gray) and 2000 UTC (black) 19 Jul 2006. The data are derived from a MGAUS sonde released at Windy Point at 2014 m MSL on the south side of Mt. Lemmon. The lifting condensation level (LCL) is shown for both soundings, as well as the elevation of Mt. Lemmon. To see more detail in the profile of relatively weak winds, two full barbs are set to correspond with  $5 \text{ m s}^{-1}$ , double the standard convention.

According to (9), the net change of moist static energy (I) expressed per unit volume over the mountain equals the horizontal convergence of sensible heat (II), the horizontal convergence of latent heat (III), the horizontal convergence of potential energy (IV), the vertical flux convergence of  $h$  (V), and any diabatic heat sources (VI). Terms II and III are controlled by MC, slightly modulated by variations in temperature and water vapor, respectively, along the track. Term IV is negligible if the average height of the stations or of the aircraft along the flight loops is set to zero. Term VI is mainly due to surface sensible and latent heating mixed into the CBL. This term typically is far smaller than the horizontal heat convergences (terms II and III) near the surface. But in a control volume centered over the mountain, horizontally confined by the surface stations and vertically confined by a capping layer above the CBL (Fig. 1), the net horizontal heat convergence is far smaller in magnitude than that either near the surface or that in the upper CBL. Thus, a net change in  $h$  (term I) in the CBL over the mountain may be dominantly affected by the surface heat flux (term VI). In this paper, we examine the surface heat flux (term VI) and the horizontal convergence (terms II and III). We only display horizontal mass convergence (MC), inferred from surface and aircraft data, because terms II and III are essentially proportional to MC.

#### 4. Case studies of mountain-scale convergence and surface heating

We now illustrate the evolution of mass and moisture convergence and cumulus growth for three days in CuPIDO. In each of the three cases cumulus congestus grew over the mountain up to a height of 9–12 km MSL and clouds aloft glaciated. One case produced a benign, short-lived thunderstorm (Cb). None of the CuPIDO cases were cloud free.

To compare  $\bar{v}_n$  values and resulting mass and energy convergence values from aircraft data with those from station data, the station data are low-pass filtered to 20 min, the time needed to complete the WKA outer loop. The evolution of  $\bar{v}_n$  and convergence is interpreted in terms of local surface heat fluxes and the profiles of stability and wind.

We characterize static stability by considering profiles of  $\theta_e$  and the saturated equivalent potential temperature ( $\theta_e^*$ ), as in Fig. 4. The  $\theta_e$  is conserved for a closed, pseudoadiabatic dry or saturated air parcel. The  $\theta_e^*$  is not conserved; it corresponds to a hypothetically saturated atmosphere and depends only on temperature. Regions where  $\theta_e^*$  decreases with height are conditionally unstable, and regions where  $\theta_e$  decreases with height are potentially unstable. The spread between  $\theta_e$  and  $\theta_e^*$  is a measure of the ambient humidity. The amount of convective available potential energy (CAPE) can be estimated as the vertically integrated

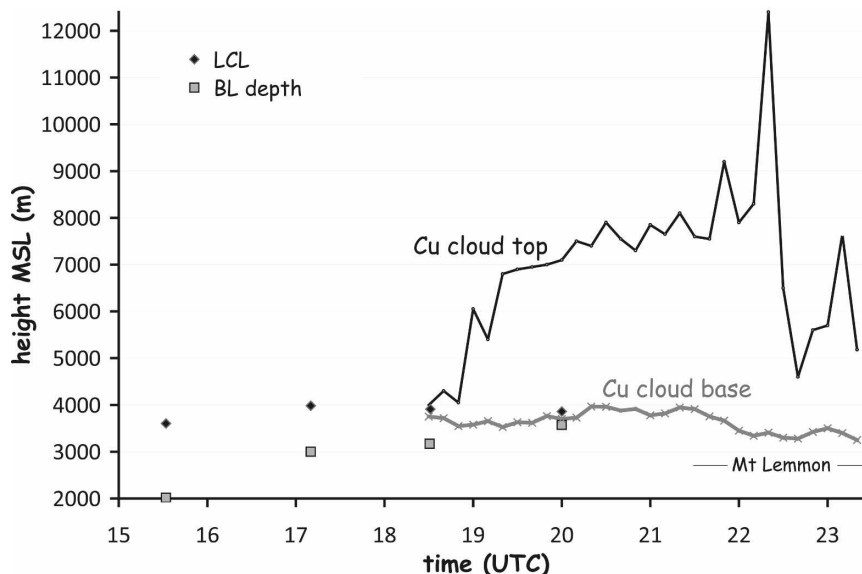


FIG. 5. Evolution of the depth of orographic cumuli over the SCM on 19 Jul 2006. Also shown are the height of the mountain, the LCL, and the depth of the convective BL. The latter two are inferred from the MGAUS soundings. The LCL is computed assuming an air parcel mixed adiabatically in the lowest 500 m.

positive difference between the BL  $\theta_c$  and the  $\theta_c^*$  profile. The CBL depth is defined as the base of the layer within which  $\theta$  increases by at least 1 K, and this increase is sustained. The radiosonde release sites were chosen to be just upstream of the mountain, such that some sondes would ascent through orographic cumuli.

a. 19 July 2006

This day started off more stable than the other two days, with virtually no potential instability in the 1532 UTC sounding (Fig. 4). This sounding, released 3 h after sunrise, reveals no mixed layer at Windy Point, a rocky outcropping at the south end of the SCM spine about 1200 m above the Tucson valley floor. In general, the wind was light and variable at most levels (Fig. 4), except for a strong easterly flow below mountain top and below a stable layer, topping at 2.5 km MSL in the 1532 UTC sounding.

By 2000 UTC [about 30 min after local solar noon (LSN)], the CBL reached 3.6 km MSL (~2.8 km above the valley floor), deeper than observed at any time on the three days, but the CAPE was only  $535 \text{ J kg}^{-1}$ . Orographic cumuli had a high cloud base compared to the other two days (Fig. 5). The CBL was not strongly capped at this time (Fig. 4). Shallow cumuli first formed 1 h before LSN, and they rapidly transitioned to cumulus (Cu) congesti (Figs. 6a–c), topping near 7 km MSL (Fig. 5), where they were capped by a stable layer (Fig. 4). By 2200 UTC two successive towers grew deeper;

the second of these produced an anvil, lightning, and brief precipitation at Mt. Lemmon (Fig. 6d).

Divergent drainage flow was commonly recorded by the Integrated Surface Flux Facility (ISFF) stations around sunrise, and mean anabatic surface flow ( $\bar{v}_n > 0$ ) developed some time after sunrise. On 19 July this occurred relatively late in the day (~5 h after sunrise), and the anabatic wind remained weak and variable throughout the day (Fig. 7d). On average the surface flow was marginally convergent during the 4 h centered on LSN (Table 1). No enhanced convergence occurred during the 2 h that the Cu congesti were trapped by the 7 km MSL stable layer (1930–2130 UTC; Fig. 5). During the development of the cumulonimbus (Fig. 5) the mountain-scale surface flow was *divergent*, and strong divergence ( $>2 \times 10^{-4} \text{ s}^{-1}$ ) occurred around 2300 UTC (Fig. 7a), due to the outflow of the decaying thunderstorm, evident in surface station data.

Most WKA loop data were collected before the first orographic Cu. Stronger anabatic flow occurred at 300 m AGL than at the surface (Fig. 7e), and the 300 m AGL convergence intensified before the first Cu appeared (Fig. 7a). Four loops were flown at 780 hPa, all within the developing CBL, all before orographic cumulus development. In all four 780-hPa loops the flow was weakly divergent (Fig. 7e). Four 700 hPa loops were flown as well. Only the last one of these was within the CBL, at the time that Cu congestus was present (Fig. 5). The flow was strongly divergent for this last loop.



FIG. 6. Snapshots of cumulus evolution on 19 Jul 2006 from camera CC6 located on the campus of the University of Arizona at (a) 1900, (b) 2010, (c) 2120, and (d) 2220 UTC.

Between 1800 and 2000 UTC (around the time of first Cu growth) a profile of low-level convergence, midlevel (780 hPa) nondivergence, and upper-CBL divergence emerges (Fig. 7a). This is evidence for the presence of a toroidal circulation within the CBL. The timing of the low-level mass convergence (Fig. 7a) on 19 July suggests that it could explain the observed orographic cumulus development. However, this convergence was weak and intermittent.

Cumulus convection could also have been initiated by local surface heating, so we examine the trend of SH (Fig. 7h). First, SH became positive  $\sim 75$  min after sunrise and remained positive throughout the day, with a magnitude of about 3 times LH, as soils were quite dry on 19 July. Thus, local surface heating over the mountain preceded the horizontal mass convergence on 19 July by several hours. While the mountain-scale convergence associated with the toroidal circulation was weak and intermittent during cumulus formation and growth, SH was strong, averaging  $200 \text{ W m}^{-2}$  (Table 1).

Clearly the development of a short-lived cumulonimbus (Cb) was not the result of low-level convergence, as the surface flow was divergent at that time. Instead, it probably resulted from the weakening of a stable layer near 7 km MSL, possibly because of sustained surface heating.

#### *b. 25 July 2006*

The last day of a relatively dry spell around the SCM was 25 July 2006 (Damiani et al. 2008). The CAPE in the 1945 UTC sounding ( $1560 \text{ J kg}^{-1}$ ; Fig. 8) was nearly 3 times that on 19 July (at 2000 UTC, Fig. 4), and the sounding-derived LCL was some 500 m lower than on 19 July (Fig. 9). The first Cu in the developing CBL over Mt. Lemmon formed at 1730 UTC, 1 h earlier than on 19 July. By 1810 UTC, shallow cumuli were present along the SCM spine (Fig. 10a). This CBL was well capped by a stable layer with strong potential instability (Fig. 8), because of a dry layer between 3 and 4 km MSL. This stable layer (evident in the 1600 UTC

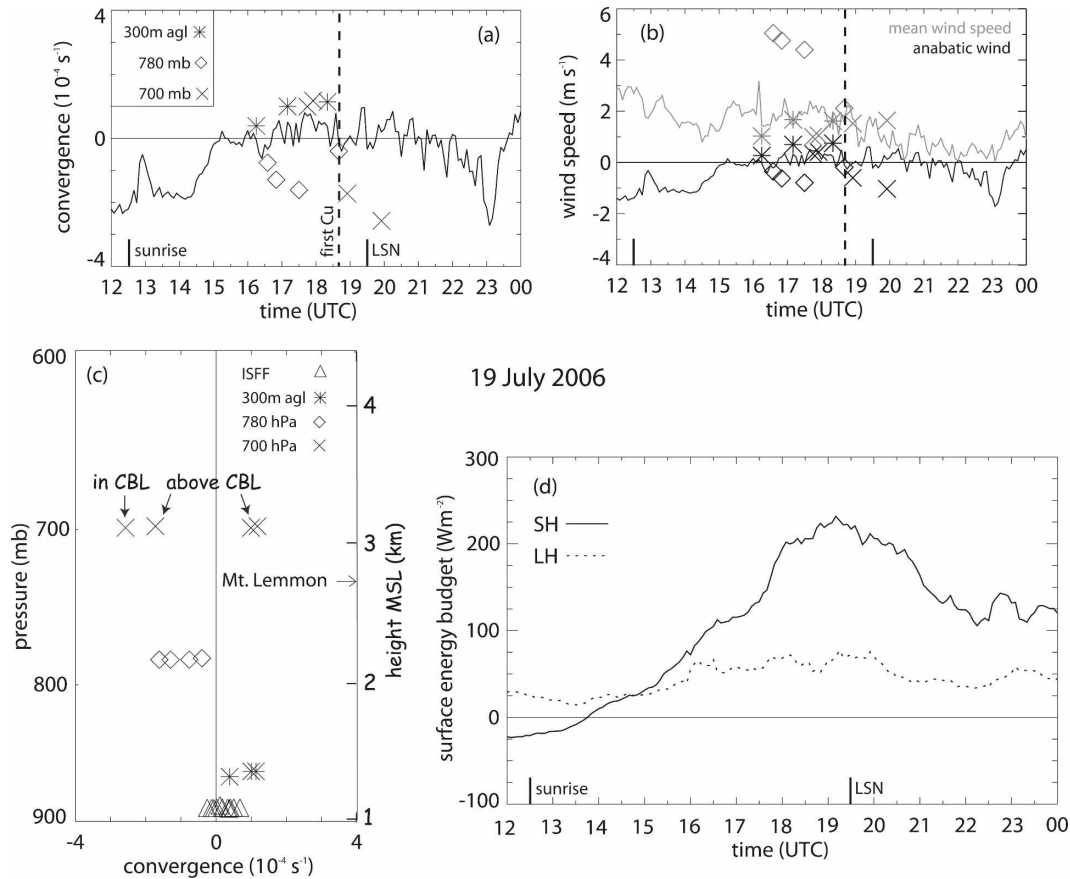


FIG. 7. Evolution of (a) mass convergence [Eq. (2)] and (b) wind on 19 Jul 2006 over the SCM. The solid line is based on 10 ISFF stations; the symbols apply to aircraft measurements at three levels. Sunrise, local solar noon, and time of first Cu are shown. In (b), both the anabatic wind [Eq. (4)] (black line and symbols) and the mean wind speed (gray line and symbols) are shown. (c) Mass convergence profile from surface and airborne measurements. The surface measurements represent 20-min averages at times corresponding to each of the aircraft loops. (d) Average surface sensible and latent heat flux for the four surface flux stations shown in Fig. 2.

sounding) suppressed cumulus growth for 1 h (Fig. 9), but it was weaker in the sounding released at 1900 UTC (not shown), at which time a Cu tower was growing rapidly (Figs. 9 and 10b).

The soundings were released from the dry, eastern

TABLE 1. Mass and heat fluxes over the SCM averaged for a 4-h period centered on LSN. The data are based on 10 stations shown in Fig. 2, except the surface flux data, which are based on four stations. The variables are defined in section 3. The CBL depth  $z_i$  is inferred from soundings (e.g., Fig. 5), and is expressed as height above the valley floor.

	19 Jul	25 Jul	6 Aug
Adiabatic flow $\bar{v}_n$ (m s <sup>-1</sup> )	0.02	1.1	0.4
Mass convergence MC (10 <sup>-4</sup> s <sup>-1</sup> )	0.2	1.8	0.7
CBL depth $z_i$ (km)	2.6	1.4	1.5
Surface sensible heat flux SH (W m <sup>-2</sup> )	200	225	140
Surface latent surface flux LH (W m <sup>-2</sup> )	60	30	190

side of the mountain; hence, the sounding-inferred LCL was higher than the observed cloud base (Fig. 9). Aircraft and surface data indicate that higher dewpoint values occurred on the west side, as mentioned in section 2 (Fig. 2). Even though the prevailing flow was from the northeast (Fig. 8), the low cloud base suggests that the orographic circulation incorporated more humid air from the west, as suggested by the low-level anabatic flow along the outer loop in Fig. 2.

The soundings reveal a moist layer between 6 and 7 km MSL (Fig. 8). Altocumulus associated with this layer was present all morning and slowly cleared without entirely disappearing. This layer was not as stable as on 19 July (Fig. 8), and the towering Cu (shown in Fig. 10b) rapidly penetrated this layer and grew to a depth of 11 km MSL in just 30 min, without producing lightning or measurable rain on the ground. The resulting anvil blew to the southwest, obscuring the view of

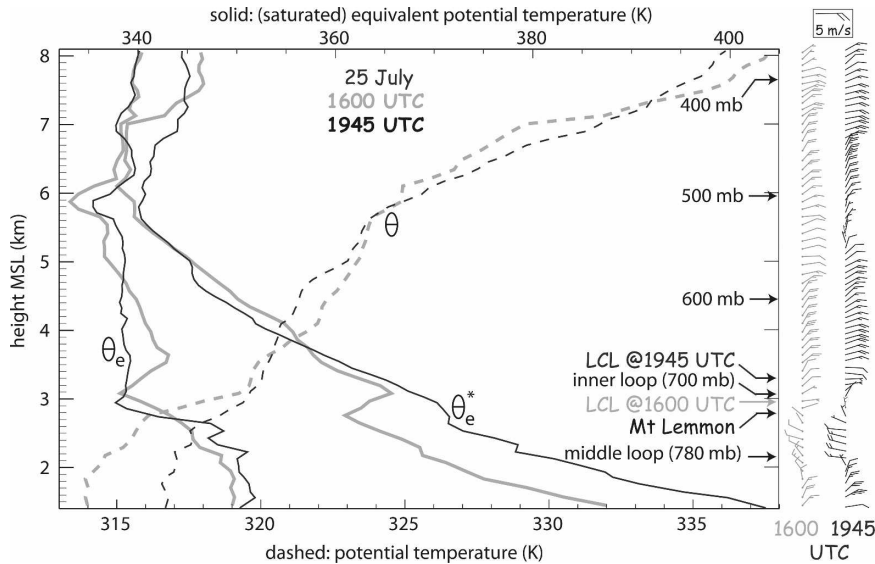


FIG. 8. As in Fig. 4, but at 1600 (gray) and 1945 UTC (black) 25 Jul 2006. The radiosondes were released from Stratton Canyon at 1390 m MSL on the east side of Mt. Lemmon.

the CC6 camera in Tucson, Arizona (Fig. 10c). A sequence of Cu towers billowed over Mt. Lemmon during much of the afternoon, with anvils spreading toward CC6 (Fig. 10d). The CBL depth remained shallower and better capped than on 19 July, according to all MGAUS soundings (Fig. 9) and the 0000 UTC Tucson sounding (not shown).

Surface data indicate that the anabatic flow commenced earlier than on 19 July, ~70 min after sunrise, and was sustained all morning into the early afternoon

(Fig. 11a). Convergent flow commenced at about the time that the surface first became a heat source (see the SH curve in Fig. 11d). It takes some time for this heat to mix vertically and develop a deep CBL, thus heating of the elevated CBL by the underlying surface could not have been the dynamic source of the early mountain-scale convergence. This convergence may have been quite shallow initially. While the SH was suppressed until ~1700 UTC due to the altostratus, mass convergence was strong before that time (Fig. 11a), and

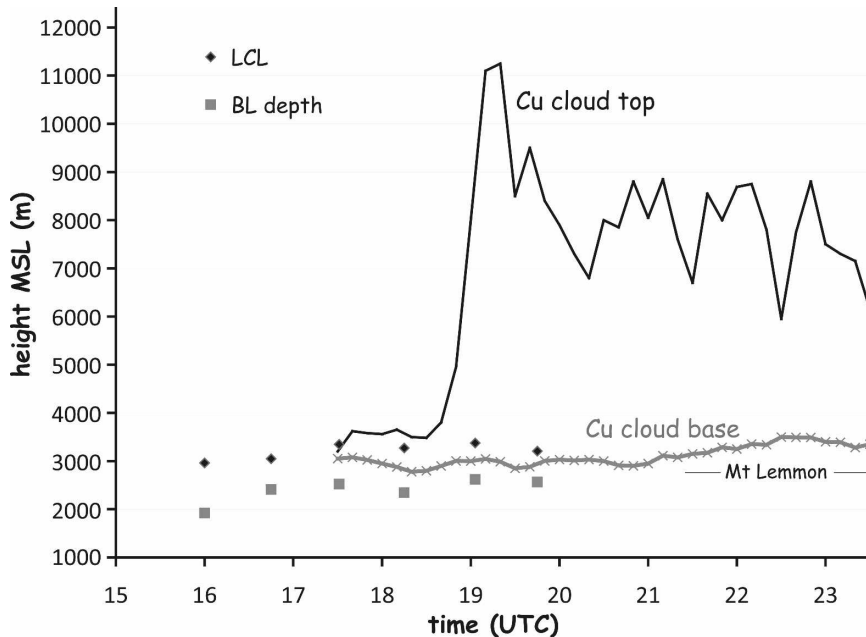


FIG. 9. As in Fig. 5, but for 25 Jul 2006.

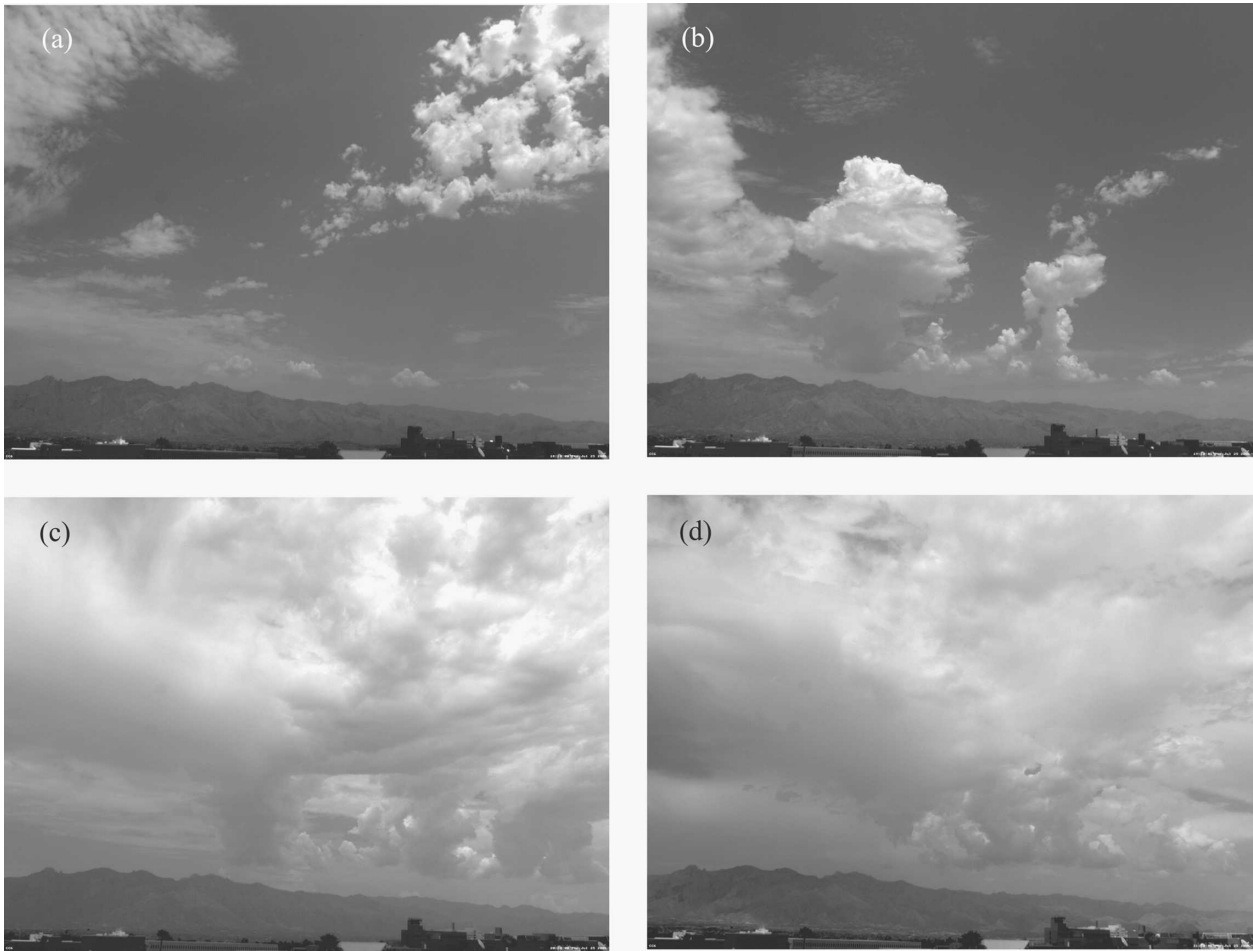


FIG. 10. As in Fig. 6, but at (a) 1810, (b) 1910, (c) 2020, and (d) 2130 UTC 25 Jul 2006.

before the first Cu appeared over Mt. Lemmon. It remained strong throughout the day (Table 1). For many hours the anabatic wind was stronger than the mean advective wind (Fig. 11b). Only six loops were flown around the mountain, and most were flown before the first orographic Cu formed. The aircraft data indicate convergent flow at all levels (Fig. 11c), although generally a bit weaker than at the surface. The lone upper-level loop showed convergence; however, it was above the CBL (Figs. 2 and 8). This is the kind of convergence indicated by the dashed arrows in Fig. 1, although it occurred before the first Cu. Ignoring this data point, a linear fit through the convergence profile (Fig. 11c) indicates a decrease with height, as on 19 July.

In summary, surface anabatic flow started earlier than on 19 July and remained strong. A toroidal circulation within the CBL was not documented on this day. It may have been present but we lack aircraft data in the upper CBL. Low-level convergence did intensify as the deep Cu congestus formed (Fig. 11a), and continued as a series of isolated Cu congesti followed over Mt.

Lemmon. Since Mt. Lemmon was just above the ambient CBL top (Fig. 11c), it appears that the anabatic flow broke through the CBL near the mountain top. The high CAPE sustained a sequence of Cu congesti, which deposited CBL air into the free troposphere, leading to a buildup of cloud debris in the already moist detrainment layer between 7 and 8 km MSL (Figs. 10c,d). A divergent cold pool containing entrained midtropospheric or evaporatively cooled air did not form over the mountain, possibly because of the stable layer on top of the CBL.

### c. 6 August 2006

On 26 July an unusually wet spell started, with dewpoint values well above average (Damiani et al. 2008). The first day since the start of this spell that the daily-mean surface dewpoint dipped below the climatological average and the early-morning sky was clear was 6 August. The MGAUS soundings reveal mostly weak and variable winds (Fig. 12) over the depth of the Cu congesti that formed over the mountain in the early after-

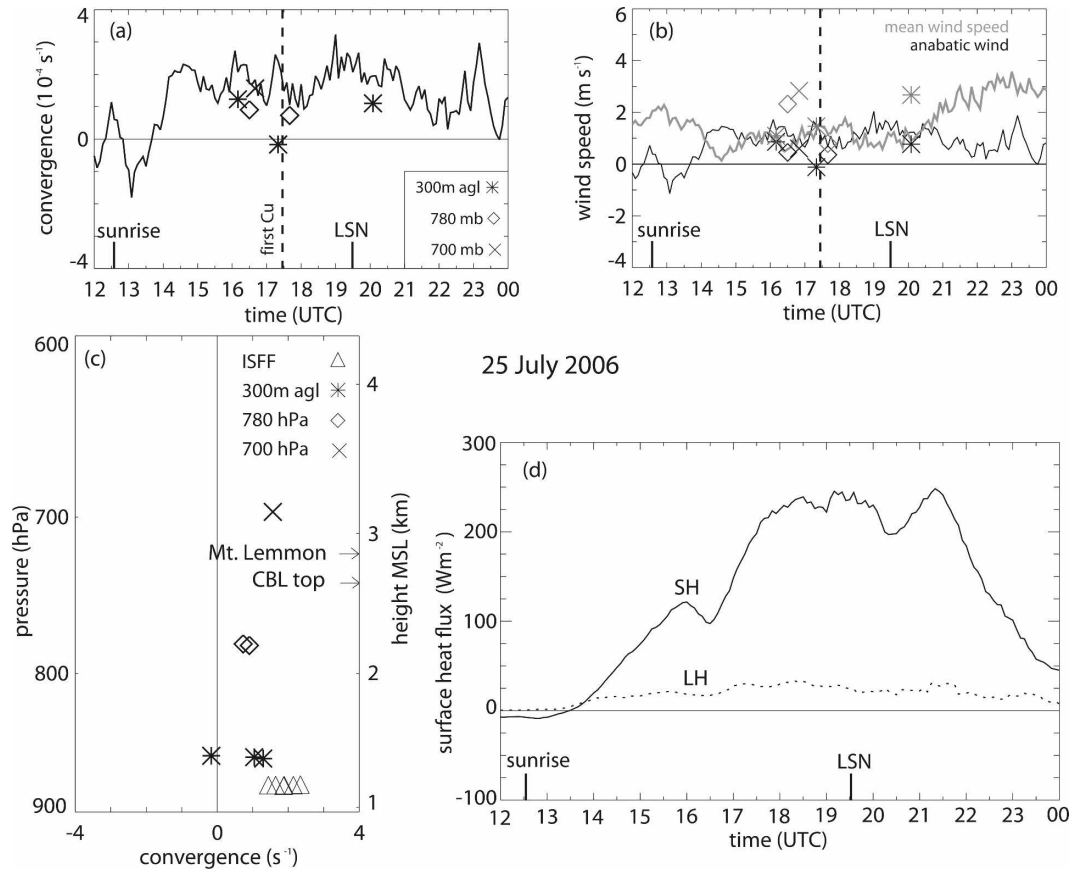


FIG. 11. As in Fig. 7, but for 25 Jul 2006.

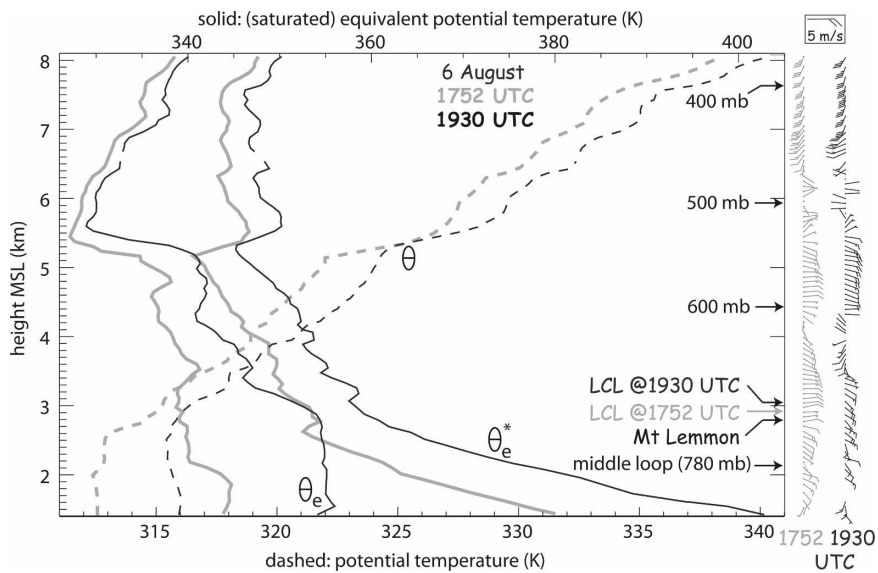


FIG. 12. As in Fig. 4, but at 1752 (gray) and 1930 UTC (black) 6 Aug 2006. The radiosonde was released from Stratton Canyon.

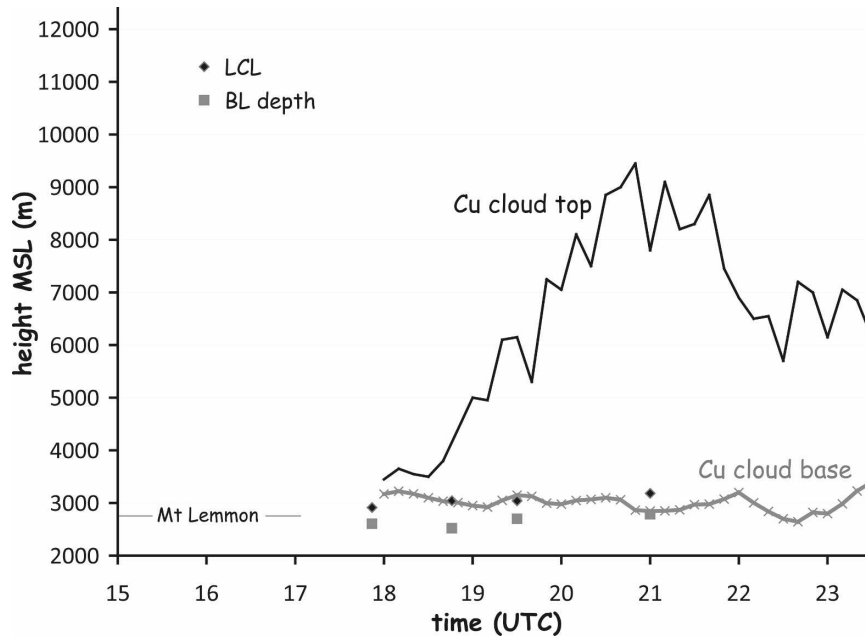


FIG. 13. As in Fig. 5, but for 6 Aug 2006.

noon (Fig. 13). A sounding released during the Cu congestus growth phase reveals a CAPE value of just  $720 \text{ J kg}^{-1}$ , and essentially no convective inhibition (Fig. 12, 1930 UTC sounding). Two layers of potential instability were present at 1930 UTC, one above the CBL and one near 5.5 km MSL (Fig. 12). A weakly stable layer between 7 and 9 km MSL blocked further growth of the Cu congesti.

The first orographic Cu formed fairly late (1800 UTC; Fig. 14a), and the cloud tops grew gradually over the course of 3 h (Figs. 14b–d). No lightning or precipitation was recorded. Because of the high soil moisture around the mountain, the daytime LH exceeded SH (Fig. 15d; Table 1). Also, the east–west asymmetry in humidity, observed on 19 and 25 July, was absent, and the sounding LCL corresponded well with the observed cloud base (Fig. 13). The CBL depth was not much below the LCL, and nonorographic BL cumuli developed in the afternoon, mainly east of the SCM (Fig. 14d).

Anabatic flow started rather early on this day, at about the same time as when SH became positive, as on 25 July (Fig. 15b). In strength this flow was intermediate between 19 and 25 July (Table 1). In the early afternoon (2100–2300 UTC) the cloud-top heights above Mt. Lemmon waned (Figs. 13 and 14d). The last available sounding, at 2100 UTC, does not reveal any midlevel drying or stabilization compared to previous soundings on this day, thus this cloud-top decline must be related to boundary layer processes: both the surface energy fluxes (Fig. 15d) and the mass (and heat) con-

vergence (Fig. 15a) decreased during this period; the latter even became negative.

Eight loops were flown around the mountain, all *after* the first orographic Cu, unlike the 19 and 25 July cases. The outer and middle loops were within the CBL, the inner loops remained above the CBL (Fig. 15c). The five early loops (1750–1920 UTC), flown during the early Cu growth phase, indicate that the flow was convergent at low levels (consistent with surface observations during this period), nondivergent in the upper CBL (780 hPa), and divergent above the CBL (700 hPa). This is the strongest evidence yet for a toroidal circulation, partly contained within the CBL. During the Cu decay phase after 2100 UTC, another stack was flown. Strong convergence was encountered at low and midlevels, in discordance with surface measurements and the observed Cu evolution.

## 5. Discussion

### a. Orographic convergence and cumulus convection

How does the trend of mountain-scale convergence near the surface affect orographic cumulus evolution, and how do cumuli in turn affect convergence? On 19 July, convergence tended to decrease during the cumulus deepening stage, while on 25 July the rapid cumulus deepening to its maximum height for the day coincided with a period of strong convergence (Fig. 16). The main cumulus burst on 25 July was followed by three less impressive Cu growth cycles. They did not generally

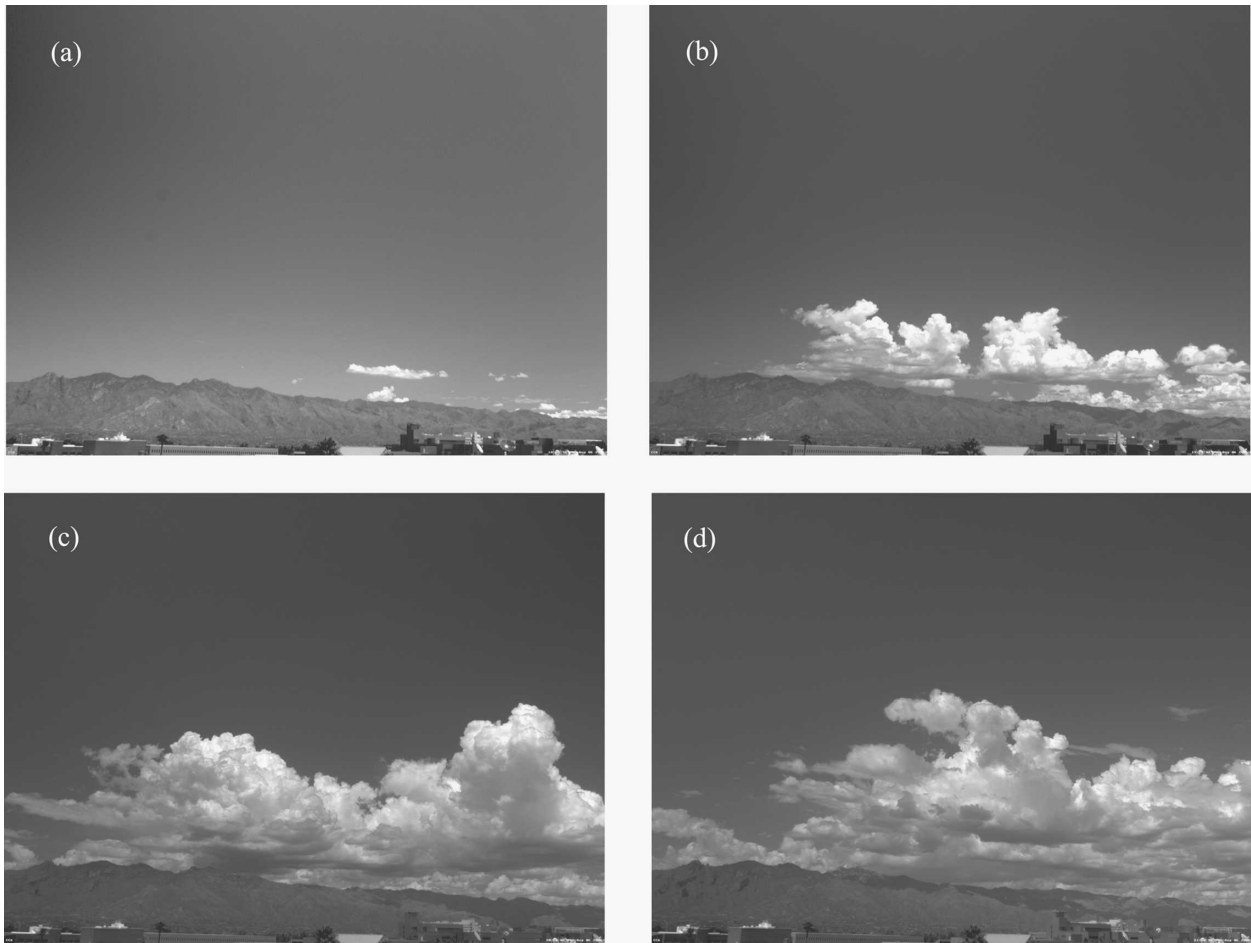


FIG. 14. As in Fig. 6, but at (a) 1810, (b) 1920, (c) 2030, and (d) 2150 UTC 6 Aug 2006.

follow (or coincide with) a convergence maximum. The only clear relationship appears to occur after a deep cumulus burst, when the convergence tends to minimize or become negative (e.g., on 19 July).

We now examine the signature of cumulus development on surface mass convergence for the 16 flight days. On each of these days orographic Cu developed, most commonly between 1600 and 1700 UTC (Fig. 17b; i.e.,  $\sim 3$  h before LSN). Orographic cumuli reached their maximum height most commonly in the first 2 h after LSN, and their peak depth was at least 4 km (i.e., they became at least Cu congesti). The Cu grew to the cumulonimbus stage, with lightning recorded close to Mt. Lemmon on 7 out of the 16 days (19 July, and 7, 9, 10, 11, 13, and 17 August).

During the 16 days, the WKA flew 24 loops around the mountain at 300 m AGL, all within the CBL, all within 3.5 h of LSN. The diurnal trend of mass convergence at the surface agrees well with the 24 convergence estimates from these flight loops (Fig. 17a), indi-

cating that surface wind data alone are sufficient to estimate the convergence within the CBL. This is important because aircraft data are relatively expensive to collect, and the number of aircraft loops flown is insufficient to reveal the diurnal trend apparent in the 16-day record.

The composite convergence (Fig. 17a) suggests that no enhanced convergence was present in the hours before Cb development, and trends for individual days confirm this: the convergence on Cb days does not substantially exceed that on congestus-only days at any time. In fact, over the course of the day, less surface convergence occurs on Cb days compared to congestus-only days. The one feature that distinguishes Cb days is that surface convergence generally vanished around LSN, with clear divergence after 2200 UTC. High variability existed amongst the seven Cb days and analysis of the individual days indicates that surface divergence generally developed shortly after the first lightning, suggesting cold pool development, as was observed in

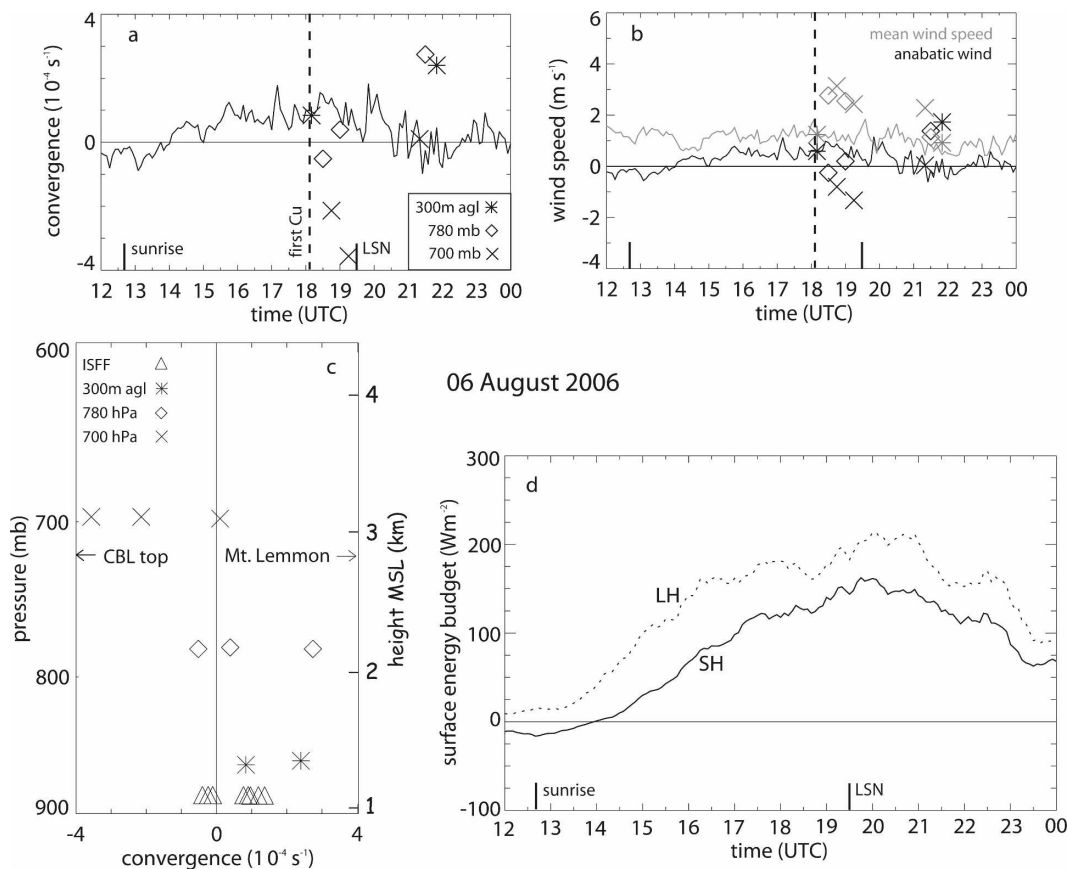


FIG. 15. As in Fig. 7, but for 6 Aug 2006.

one case by Raymond and Wilkening (1982). Thus, while thunderstorms undoubtedly transport more CBL energy and moisture into the upper troposphere than Cu congesti, surface measurements suggest that *orographic thunderstorms suppress the BL solenoidal circulation*, due to cold-pool spreading.

The weakening of the solenoidal circulation by thunderstorms is confirmed by aircraft data. The 300 m AGL flight loops support the notion of afternoon divergence on Cb days (Fig. 17a). At the midlevel (780 hPa), divergence occurs on Cb days, and convergence occurs on congestus-only days (Fig. 18). This is especially surprising since all but one 780-hPa loop on Cb days were flown before Cb occurrence. At 700 hPa no significant difference exists between Cb and congestus-only days. Mountain-scale vertical velocity ( $w$ ) can be computed from the convergence values at various levels, using air mass continuity and assuming  $w = 0$  at the surface. On congestus-only days deep rising motion is present in the CBL, peaking at  $0.21 \text{ m s}^{-1}$  or  $\sim 750 \text{ m}$  in 1 h. Because of the slope of the terrain (about 0.10 between the ISFF stations and the mountain top), and the mean anabatic flow at the surface ( $0.4 \text{ m s}^{-1}$  on

average, during the period of the congestus-only flight loops; see Fig. 17a), the peak mountain-scale vertical velocity may be slightly higher, about  $0.25 \text{ m s}^{-1}$ . Orographic ascent in the CBL is weaker and shallower on Cb days (Fig. 18). Thus, the aircraft data corroborate the conclusion reached from the surface data.

The two-month long record of ISFF data further corroborates that thunderstorms suppress the near-surface convergence: Fig. 19 contrasts the composite mountain-scale convergence on days with thunderstorms (as determined by lightning occurrence within 13 km from Mt. Lemmon between 1800 and 0000 UTC, recorded by the National Lightning Detection Network) against that on days with shallow Cu over the mountain only (as inferred from CC6 time lapse photography). Clearly the solenoidal surface convergence is suppressed on Cb days, starting around LSN, while it is sustained through the afternoon on shallow Cu days. The mountain-scale convergence starts about 1 h earlier and is more intense in the morning on Cb days, compared to shallow Cu days. The two-month record will be explored further in a separate study.

This conclusion is counterintuitive, yet it is not in-

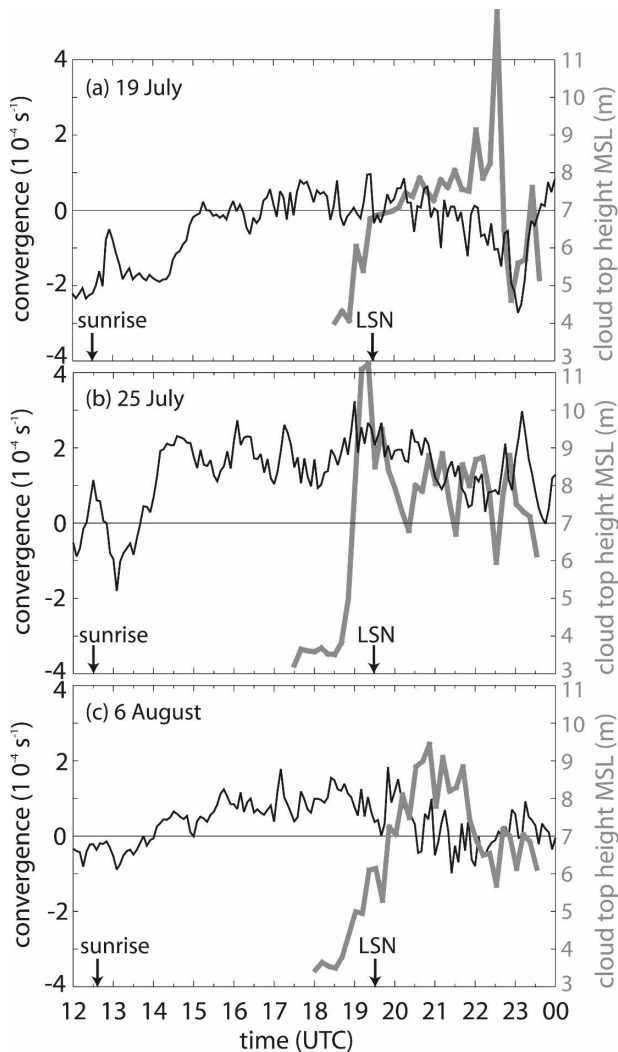


FIG. 16. Correspondence between mountain-scale convergence and orographic cumulus-top height for the three days studied herein.

consistent with the aircraft data analysis by Raymond and Wilkening (1982). While the mean anabatic flow does advect the moist static energy needed to *sustain* orographic convection, it may not explain the *onset* of orographic deep convection. In general deep convection is triggered where the CBL reaches the level of free convection, which is most likely where the CBL domes (Fig. 1). Apparently this doming is not the result of the solenoidal circulation, but rather local surface heating. In terms of eroding the convective inhibition (CIN) and maximizing CAPE, the anabatic flow does not help: it is the nature of solenoidal forcing that anabatic surface flow advects cooler air (Fig. 1) and aims to destroy the horizontal difference of virtual potential temperature ( $\theta_v$ ; see section 5b). Thus, ignoring any horizontal moisture gradients, anabatic flow lowers the

moist static energy, increases CIN, and decreases CAPE. This is consistent with the absence of enhanced anabatic flow prior to convective bursts, as discussed above.

The implications are twofold: (a) mountain-scale mass convergence near the surface cannot be used as a precursor for convective initiation over mountains, unlike in the plains (e.g., Wilson and Schreiber 1986; Wilson et al. 1992); and (b) orographic cumulus vertical growth is controlled by something else; the most likely candidate, as suggested by Zehnder et al. (2007), is the evolution of the profile of static stability, which is affected by surface heating over the mountain, or by changes aloft.

The composite surface data in Fig. 17a demonstrate that mountain-scale convergence develops about 1.5 h after sunrise, at about the same time as surface heating commences ( $SH > 0$ ; Fig. 17c). Such an early start is typical for small-scale upslope flow [p. 179 in Whiteman (2000)], but it is earlier than expected for a mountain–plain circulation of this size. This is addressed further in Geerts et al. (2008). The convergence also peaks about 2 h before LSN (the time that SH peaks) on thunderstorm days (Figs. 17a and 19), about 1 h before LSN on Cu congestus days, and about 1 h after LSN for days with shallow Cu only (Fig. 19). This shift in peak convergence time confirms that moist convection suppresses the solenoidal circulation in the CBL.

These findings are based on a small sample and need to be further corroborated. In a separate study (in progress), we examine the relationship between cloud-top evolution, moist static energy at Mt. Bigelow, and mountain-scale convergence for the 2-month period of ISFF data in CuPIDO, and statistically assess differences between different convective classes.

### b. Thermal forcing of anabatic flow

We now examine the thermal forcing of the low-level anabatic wind and the toroidal circulation. Such circulation mostly contained within the CBL (low-level convergence, upper-level divergence) appears to be present on 6 August (Fig. 15c) and on 19 July (Fig. 7e), as well as in the 16-day average profile (Fig. 18). The development of a toroidal vorticity ( $\eta$ ) around an isolated heated mountain is the result of solenoidal forcing [i.e., a gradient of buoyancy (or  $\theta_v$ ) toward the mountain (Fig. 1)]:

$$\frac{D\eta}{Dt} \equiv \frac{g}{\theta_v} \frac{\partial \theta_v}{\partial x}. \quad (10)$$

Numerical simulations have documented the development of this baroclinicity and resulting circulation

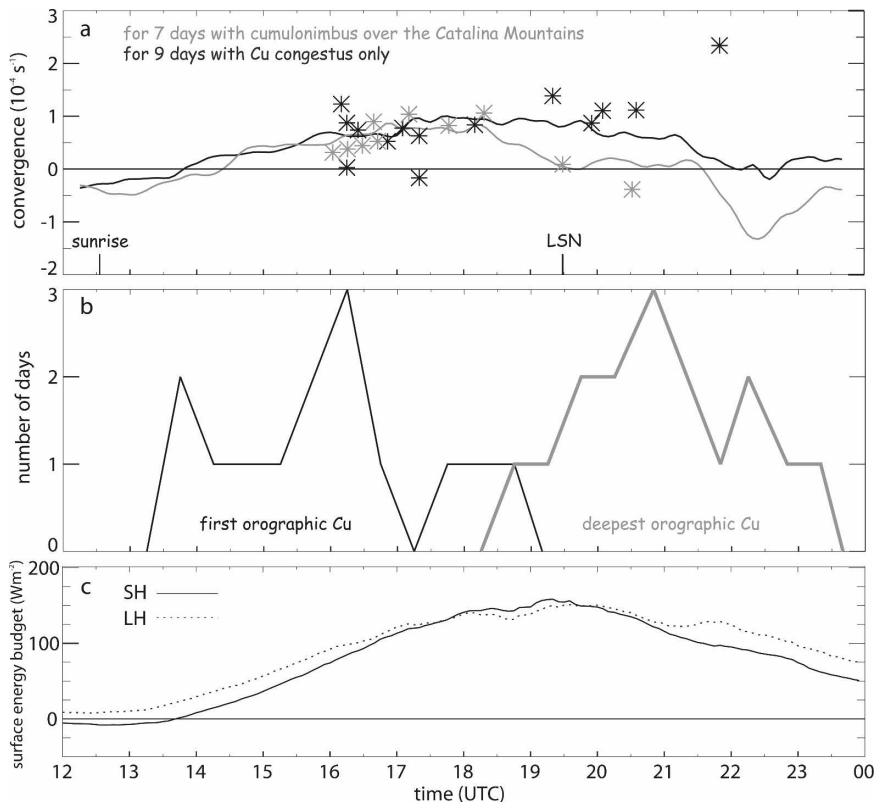


FIG. 17. (a) Diurnal variation of mass convergence on days with orographic Cb (7 days) and those with only Cu congestus development (9 days). The lines represent averages based on surface station data, and the symbols represent 24 loops flown at 300 m AGL. (b) Diurnal variation of the time of first Cu and of deepest Cu for the 16 flight days, inferred from the CC6 camera images. (c) Average surface heat fluxes for the same days.

(e.g., de Wekker et al.1998). Therefore we examine the variation of  $\theta_v$  in a vertical cross section on the 3 days studied in section 4 (Fig. 20). The terrain profile is an average in all four wind directions, starting at Mt. Lemmon, but clearly the azimuthal symmetry is significant (e.g., Fig. 3). All aircraft and surface station data are plotted as a function of their distance from Mt. Lemmon. The vertical position of all data is their height MSL, rather than their height above the indicative terrain, because the solenoidal forcing needs to be evaluated on constant pressure surfaces. This places some surface stations “underground.” In most cases the upper flight loop data are collected above the CBL, as is evident from the  $\theta_v$  profiles (Figs. 20b,d,f). Thus, to reveal radial differences,  $\theta_v$  perturbations are plotted. The perturbation  $\theta_v$  is defined as the departure from the mean at any of the three flight levels, or from the mean of the 10 surface stations. Data from the Bigelow flux tower are included (the triangle at 2583 m MSL in Fig. 20). For this site the perturbation  $\theta_v$  is defined as the departure from the mean  $\theta_v$  at the 780-hPa flight

loop, because that flight level comes closest to the elevation of Mt. Bigelow. The aircraft data were filtered to 10 s ( $\sim 800\text{-m}$  along-track distance) and the 5-min station data were averaged to match the time needed to collect all aircraft data. The radial extent of the data is somewhat limited because of the flight patterns and the distribution of surface stations. Mt. Bigelow is on a ridge at 6.6 km to the southeast of Mt. Lemmon; thus, it appears much higher than the average terrain height.

One common aspect for the three cross sections in Fig. 20 is that Mt. Bigelow has a  $\sim 2 \text{ K}$  higher  $\theta_v$  than at the 780-hPa flight level, including 19 July and 6 August, when the CBL top clearly was above the elevation of Mt. Bigelow. This is true also for other cross sections of combined multilevel aircraft data and station data (not shown), except one, at 2113–2201 UTC 6 August, presumably because of a cold pool development associated with cloud-top subsidence and divergent flow in the CBL (Fig. 16). One may argue some instrument calibration problem at Mt. Bigelow, so we compared the Bigelow  $\theta_v$  values to those just above the surface in

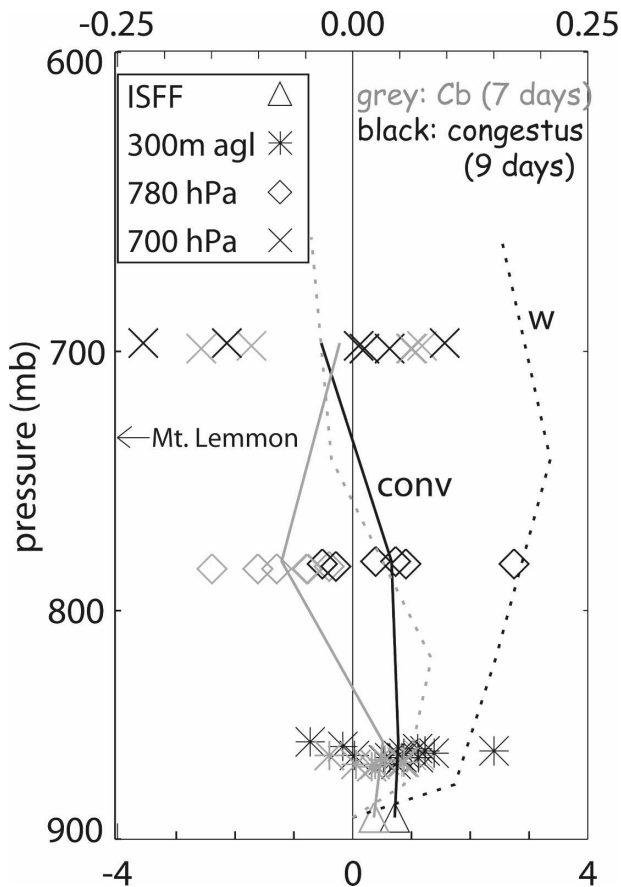


FIG. 18. Mass convergence profiles for the same days as in Fig. 17. The solid lines represent the average convergence profiles for Cb days and congestus days. The two ISFF measurements represent the time-averaged surface station measurements during the period of aircraft measurements, which occurred between 1600 and 2200 UTC. The dotted lines are vertical velocity ( $w$ ) profiles derived from the convergence profile, assuming  $w = 0$  at the ground.

soundings released from both Windy Point and Mt. Lemmon (locations are shown in Fig. 3) at several times when the CBL was well developed and deep. These values corresponded well. This yields evidence of a *warm core over the mountain*.

Otherwise, the aircraft and surface data do not reveal a clear pattern of warmer air ( $\theta'_v > 0$ ) closer to the mountain. In essence, the station layout and flight pattern were not ideal to measure solenoidal forcing: a long line of stations and low-level, terrain-following flight tracks across the mountain would be superior. The large azimuthal asymmetry of  $\theta$  on 25 July (Fig. 2) explains the large variations in  $\theta'_v$  seen in Fig. 20c, especially for the lower, outer loop. Aircraft data give some indication for the expected baroclinicity on 6 August (Fig. 20e). This series of loops was flown later than the others and closer to LSN. Certainly the difference

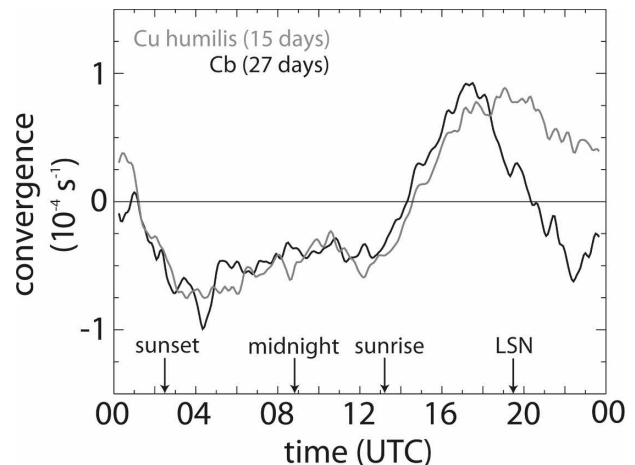


FIG. 19. Diurnal variation of the mountain-scale convergence, inferred from the 10-station polygon (Fig. 3), for 15 days with shallow orographic cumuli (gray line), and for 27 days with lightning over the SCM between 1800 and 0000 UTC (black line) between 22 Jun and 29 Aug 2006.

in observed surface convergence strength (Fig. 16) cannot be explained by differences in the  $\theta'_v$  distribution (Fig. 20). We also plotted the data points at the observed height MSL, with their distance from Mt. Lemmon determined by the condition that their plotted height above the average terrain profile equals the actual height AGL. This method redistributes the data and does reveal the expected baroclinicity more clearly, especially in two cross sections on 25 July (Fig. 21), when the anabatic flow was the strongest. Here the aircraft data suggest a radial  $\theta'_v$  gradient of roughly  $1 \text{ K} (10 \text{ km})^{-1}$ , with warmer air closer to the mountain.

### c. Hydrostatic pressure variations and anabatic flow

There is another way to detect the presence of warmer BL air closer to the mountain. Hydrostatic balance implies that a higher temperature over some depth in the atmosphere is associated with a lower pressure below this layer. Using typical values for the SCM (in particular, a CBL depth of 1.6 km), a temperature excess of 2 K over the mountain yields a hydrostatic pressure deficit of 1.0 hPa, assuming a flat CBL top. Since the reference level is the foothills around the mountain, this lower pressure would occur under the mountain bedrock, but the pressure gradient force is nevertheless real.

Observed pressure perturbations for the three days studied herein are shown in Fig. 22. The pressure perturbation is defined as in Fujita et al. (1962) (i.e., the daily average value is removed, to eliminate the effect of station elevation). Fujita et al. (1962), examining a

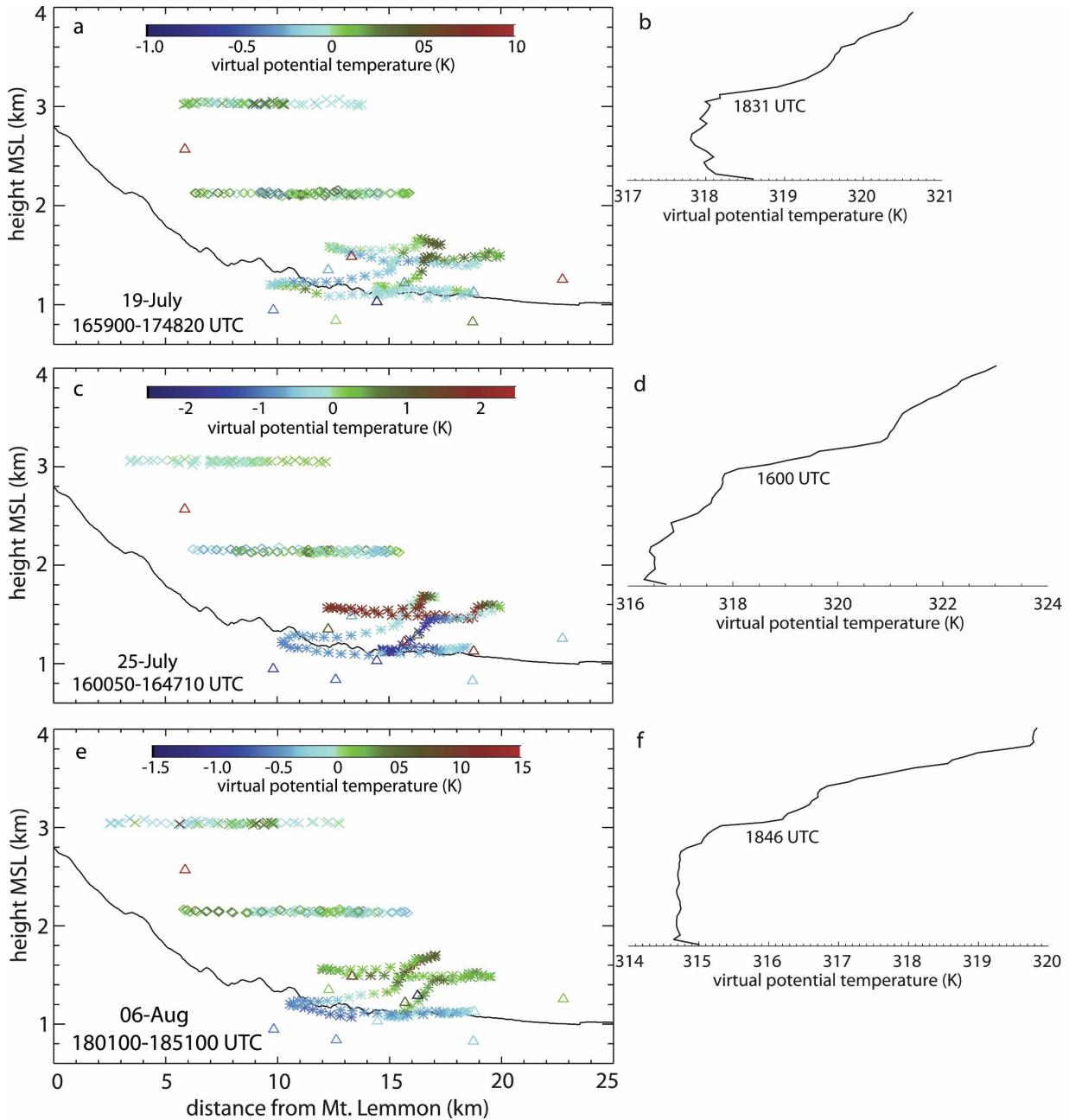


FIG. 20. (left) Cross sections of virtual potential temperature  $\theta_v$ , expressed as a perturbation from the mean value at any of the three flight levels or at the surface. Aircraft data from the three loops are shown with distinct symbols, and surface data are shown as triangles. The solid black line is an indicative, average terrain profile. (right) The  $\theta_v$  profile from a sounding released around the time that the data in the left panels were collected. They have the same vertical axis as the left panels. (top), (middle), and (bottom) are for 19 Jul, 25 Jul, and 6 Aug 2006, respectively.

mountain of similar relative height as the SCM, assume that the resulting perturbation pressure gradients can be interpreted as *horizontal* pressure gradients. Geerts et al. (2008) show that a temperature-dependent correction is needed to obtain horizontal pressure gradients that drive horizontal wind. To reveal anabatic and

katabatic forcing, we have plotted the difference of this pressure perturbation at any station with that at Mt. Bigelow (Fig. 22). Positive differences imply lower pressure over the mountain, thus anabatic forcing.

A clear stratification with station height is obvious: a larger pressure difference exists at lower stations (in

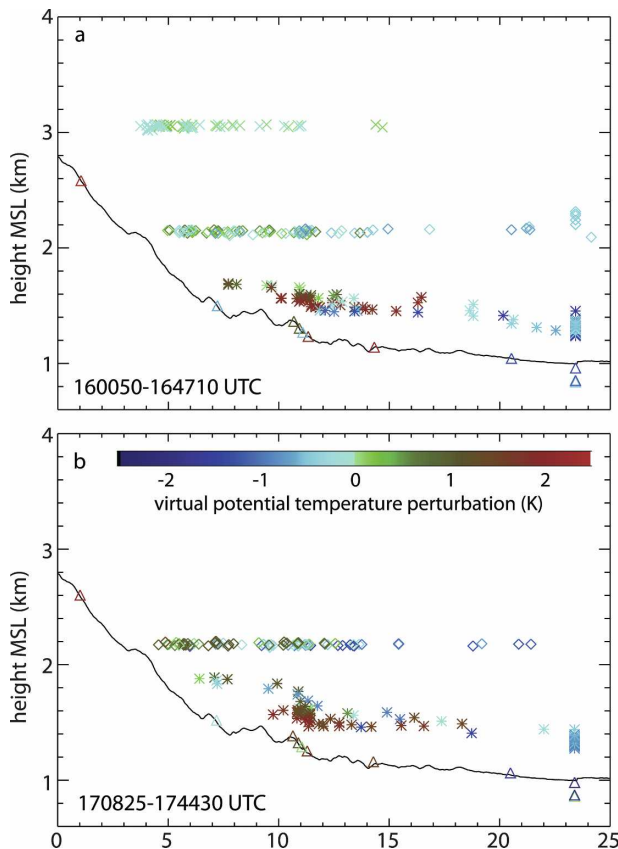


FIG. 21. Cross sections of virtual potential temperature,  $\theta_v$ , based on aircraft and station data, for 25 Jul 2006, for (a) 1601–1647 and (b) 1708–1745 UTC. As in Fig. 20, the actual height MSL of the observations is shown, but unlike in Fig. 20, the  $x$ -axis value is the distance at which the actual height above the ground optimally corresponds with the height above the average terrain profile (black line).

red). Assuming a bell-shaped mountain, these lower stations are also further away, thus the pressure *gradient* (toward or away from the mountain) varies little between stations. On each of the three days, katabatic forcing prevails at night. Anabatic forcing prevails during the day, starting about 2 h after sunrise, and peaking close to LSN. The average anabatic forcing is about equally strong on the three days, in other words the differences in anabatic flow development between 19 and 25 July cannot be explained by differences in the independently derived horizontal pressure gradient. Nevertheless the general, low-pass-filtered pattern of anabatic flow evolution matches the average anabatic pressure forcing pattern on each of the three days, suggesting that the flow rapidly responds to the pressure forcing, as expected from Eq. (10). Also, the magnitude of the pressure difference, about 1 hPa, and the magnitude of the observed temperature excess at Mt. Bigelow at times that this station is within the CBL ( $\sim 2$  K,

see e.g., Figs. 20a,e) confirm that this pressure difference is hydrostatically driven by a temperature difference in the CBL. The katabatic flow spike associated with a thunderstorm outflow on 19 July (Fig. 22b) is not present in the pressure forcing, possibly because the cold pool is too shallow. Using a 2-month composite of horizontal pressure perturbation differences between the 10 ISFF stations and Mt. Bigelow, Geerts et al. (2008) find good temporal correspondence between anabatic forcing and anabatic flow.

## 6. Conclusions

Surface and aircraft data collected over the Santa Catalina Mountains in Arizona were used to study the development of mass and heat convergence over an isolated heated mountain, and their relation to orographic convection. This study focused on 3 days, and included an additional 13 days, each with Cu congestus or Cb development over the mountain. The main findings are as follows:

- Aircraft data collected along a closed loop around the mountain in the lower CBL indicate that mountain-scale convergence can be well estimated using data from a series of surface stations around the mountain.
- An orographic toroidal circulation with low-level anabatic flow and divergence near the CBL top is sometimes, but not always, present prior to orographic cumulus development.
- Station data indicate that mountain-scale convergence typically develops shortly after sunrise and peaks close to local solar noon. The anabatic flow is driven by surface heating over the mountain, resulting in solenoidal forcing and a hydrostatic horizontal pressure gradient force toward the mountain.
- Orographic cumulus and cumulonimbus development are not triggered by mountain-scale mass convergence near the surface, but rather probably by local surface heating; in fact convergent flow may suppress the initiation or deepening of convection over mountains. This does not mean that the low-level convergence of moist static energy by the anabatic flow is not essential for the maintenance of orographic convection. Surface flow tends to be katabatic following a thunderstorm outbreak over the mountain.

The last two conclusions will be corroborated in a follow-up study using two months of station data, collected as part of CuPIDO, and results will be stratified as a function of stability, thunderstorm development, and soil moisture. Another follow-up study will com-

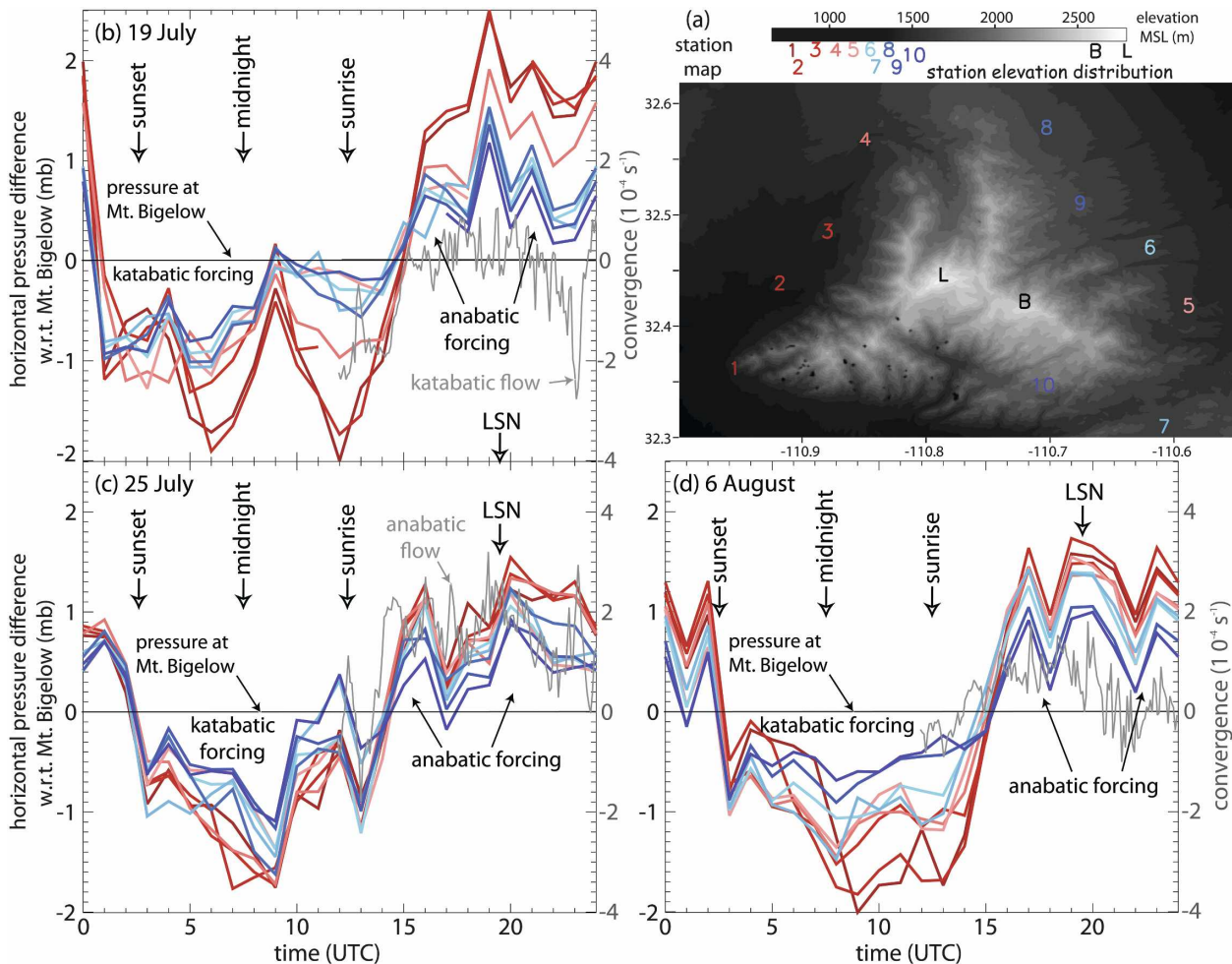


FIG. 22. Horizontal pressure perturbation differences between 10 ISSF stations and Mt. Bigelow for the 3 days studied herein: (b) 19 Jul, (c) 25 Jul, and (d) 6 Aug 2006. (a) The location and height distribution of the stations is shown. The stations are color coded, the lowest ones in red, and the higher ones in blue. Note that a 24-h period is shown, unlike in previous figures. The pressure perturbation is defined in the text. The mountain-scale convergence traces (gray lines; also shown in Fig. 16) are superimposed for comparison.

pare the above conclusions with those arising from detailed numerical simulations.

*Acknowledgments.* CuPIDO was funded by National Science Foundation (NSF) Grants ATM-0444254, ATM-035298, and by the NSF facility deployment pool. Special thanks go to the WKA, ISFF, and MGAUS crews during the CuPIDO field phase. We appreciate the review comments of Thomas Parish and three anonymous reviewers.

REFERENCES

Ackerman, S. A., and J. A. Knox, 2007: *Meteorology: Understanding the Atmosphere*. 2nd ed. Thomson, 464 pp.  
 Aguado, E., and J. E. Burt, 2007: *Understanding Weather & Climate*. 4th ed. Prentice Hall, 562 pp.  
 Bader, D. C., and T. B. Mckee, 1983: Dynamical model simulation

of the morning boundary layer development in deep mountain valleys. *J. Climate Appl. Meteor.*, **22**, 341–351.  
 Banta, R. M., 1984: Daytime boundary layer evolution over mountainous terrain. Part I: Observations of the dry circulations. *Mon. Wea. Rev.*, **112**, 340–356.  
 —, 1986: Daytime boundary layer evolution over mountainous terrain. Part II: Numerical studies of upslope flow duration. *Mon. Wea. Rev.*, **114**, 1112–1130.  
 Batchelor, G. K., 1967: *An Introduction to Fluid Mechanics*. Cambridge Press, 615 pp.  
 Braham, R. R., and M. Draginis, 1960: Roots of orographic cumuli. *J. Atmos. Sci.*, **17**, 214–226.  
 Bright, D. R., and S. L. Mullen, 2002: Short-range ensemble forecasts of precipitation during the Southwest monsoon. *Wea. Forecasting*, **17**, 1080–1100.  
 Damiani, R., and Coauthors, 2008: Cumulus Photogrammetric, In-situ and Doppler Observations: The CuPIDO 2006 experiment. *Bull. Amer. Meteor. Soc.*, **89**, 57–73.  
 de Wekker, S. F. J., S. Zhong, J. D. Fast, and C. D. Whiteman,

- 1998: A numerical study of the thermally driven plain-to-basin wind over idealized basin topographies. *J. Appl. Meteor.*, **37**, 606–622.
- Fujita, T., K. A. Styber, and R. A. Brown, 1962: On the mesometeorological field studies near Flagstaff, Arizona. *J. Appl. Meteor.*, **1**, 26–42.
- Hernández, E., J. de las Parras, I. Martín, A. Rúa, and L. Gimeno, 1998: A field case study and numerical simulation of mountain flows with weak ambient winds. *J. Appl. Meteor.*, **37**, 623–637.
- Garrett, A. J., 1980: Orographic cloud over the eastern slopes of Mauna Loa Volcano, Hawaii, related to insolation and wind. *Mon. Wea. Rev.*, **108**, 931–941.
- Geerts, B., Q. Miao, and J. C. Demko, 2008: Pressure perturbations and upslope flow over a heated, isolated mountain. *Mon. Wea. Rev.*, **136**, 4272–4288.
- Holton, J. R., 2004: *An Introduction to Dynamic Meteorology*. 4th ed. Elsevier/Academic Press, 535 pp.
- Johnson, R. H., and D. L. Priegnitz, 1981: Winter monsoon convection in the vicinity of north Borneo. Part II: Effects on large-scale fields. *Mon. Wea. Rev.*, **109**, 1615–1628.
- Lenschow, D. H., and B. B. Stankov, 1986: Length scales in the convective atmospheric boundary layer. *J. Atmos. Sci.*, **43**, 1198–1209.
- , P. B. Krummel, and S. T. Siems, 1999: Measuring entrainment, divergence, and vorticity on the mesoscale from aircraft. *J. Atmos. Oceanic Technol.*, **16**, 1384–1400.
- McNider, R. T., and R. A. Pielke, 1981: Diurnal boundary-layer development over sloping terrain. *J. Atmos. Sci.*, **38**, 2198–2212.
- Raymond, D. J., and M. H. Wilkening, 1980: Mountain-induced convection under fair weather conditions. *J. Atmos. Sci.*, **37**, 2693–2706.
- , and —, 1982: Flow and mixing in New Mexico mountain cumuli. *J. Atmos. Sci.*, **39**, 2211–2228.
- , and —, 1985: Characteristics of mountain-induced thunderstorms and cumulus congestus clouds from budget measurements. *J. Atmos. Sci.*, **42**, 773–783.
- Thyer, N. H., 1966: A theoretical explanation of mountain and valley winds by a numerical method. *Meteor. Atmos. Phys.*, **15**, 318–348.
- Vergeiner, I., and E. Dreiseitl, 1987: Valley winds and slope winds: Observations and elementary thoughts. *Meteor. Atmos. Phys.*, **36**, 264–268.
- Whiteman, C. D., 1990: Observations of thermally developed wind systems in mountainous terrain. *Atmospheric Processes over Complex Terrain, Meteor. Monogr.*, No. 45, Amer. Meteor. Soc., 5–42.
- , 2000: *Mountain Meteorology: Fundamentals and Applications*. Oxford University Press, 376 pp.
- Wilson, J. W., and W. E. Schreiber, 1986: Initiation of convective storms by radar-observed boundary-layer convergent lines. *Mon. Wea. Rev.*, **114**, 2516–2536.
- , G. B. Foote, N. A. Crook, J. C. Fankhauser, C. G. Wade, J. D. Tuttle, and C. K. Mueller, 1992: The role of boundary layer convergence zones and horizontal rolls in the initiation of thunderstorms: A case study. *Mon. Wea. Rev.*, **120**, 1785–1815.
- Yu, W., Y. Liu, T. Warner, R. Bullock, B. Brown, and M. Ge, 2006: A comparison of very short-term QPFs for summer convection over complex terrain areas, with the NCAR/ATEC WRF and MM5-based RTFDDA systems. *Seventh WRF Users Workshop*, Boulder, CO, NCAR, 8.5. [Available online at [http://www.mmm.ucar.edu/wrf/users/workshops/WS2006/abstracts/Session08/8\\_5\\_Yu.pdf](http://www.mmm.ucar.edu/wrf/users/workshops/WS2006/abstracts/Session08/8_5_Yu.pdf).]
- Zehnder, J. A., L. Zhang, D. Hansford, A. Radzan, N. Selover, and C. M. Brown, 2006: Using digital cloud photogrammetry to characterize the onset and transition from shallow to deep convection over orography. *Mon. Wea. Rev.*, **134**, 2527–2546.
- , J. Hu, and A. Radzan, 2007: A stereo photogrammetric technique applied to orographic convection. *Mon. Wea. Rev.*, **135**, 2265–2277.